Version: Published Version

Article:

He, L., Zhang, Q., You, Y. et al. (2025) Exogenous activation of the adhesion GPCR ADGRD1/GPR133 protects against bone loss by negatively regulating osteoclastogenesis. Science Advances, 11 (28). ISSN: 2375-2548

https://doi.org/10.1126/sciadv.ads3829

BIOCHEMISTRY

Exogenous activation of the adhesion GPCR ADGRD1/GPR133 protects against bone loss by negatively regulating osteoclastogenesis

Liang He[1]†, Qiansen Zhang[2]*†, Yu You[1]†, Peng Sun[3]†, Ziwei Xu[2], Rong Li[1], Fanhua Wang[1], Shaoying Zhang[2], Jiangnan He[2], Juwen Shen[2], Lei Zhao[1], Yang Hong[4], Yinghua Li[4], Mingyao Liu[2], Jin-peng Sun[5,6], Ning Wang[7,8], Yeqing Sun[1]*, Huaiyu Yang[2]*, Jian Luo[1]*

Adhesion G protein–coupled receptors (GPCRs) play crucial roles in numerous physiological and pathological conditions. However, the functions of adhesion GPCRs remain poorly understood because of the lack of effective modulators. Here, we used the adhesion GPCR D1 (ADGRD1/GPR133) as a model to unveil a strategy for finding exogenous agonists that target adhesion GPCRs while revealing previously unidentified functions of ADGRD1. We identified the small molecule GL64 as a selective agonist of ADGRD1. GL64 activates ADGRD1 by mimicking the *stachel* sequence. Using GL64 as a chemical tool, we demonstrated that ADGRD1 negatively regulates bone loss by inhibiting osteoclastogenesis. The cAMP-PKA-NFATC1 pathway was identified as the downstream signaling pathway of ADGRD1 in osteoclasts. Furthermore, administering GL64 prevented bone loss and suppressed osteoclast activity in the osteoporosis mouse model induced by ovariectomy. Our findings provide mechanistic insights into the activation of adhesion GPCRs by exogenous agonists and underscore the therapeutic potential of targeting ADGRD1 in osteoclast-related diseases.

INTRODUCTION

G protein–coupled receptors (GPCRs) represent the largest and most diverse family of membrane receptors in eukaryotes, encompassing ~801 members across five principal families (*1*). These seven transmembrane receptors are central to numerous fundamental biological processes and pathologies, as evidenced by the fact that they are the target of ~30% of all drugs approved by the US Food and Drug Administration (*2*–*4*). Most of these drugs target class A GPCRs, commonly known as rhodopsin-like receptors (*5*, *6*). In contrast, adhesion GPCRs, which are similarly crucial for organ development and disease progression (*7*, *8*), lag behind in drug discovery compared with other GPCR families. Although some studies have provided structural evidence and elucidated endogenous activation mechanisms involving the tethered agonist (*stachel*) of adhesion GPCRs (*9*, *10*), progress has been limited because of the lack of suitable exogenous agonists with lower median effective concentration (EC_{50}) values and better druggability. Moreover, the limited knowledge of exogenous agonist activation mechanisms further hampers drug discovery for adhesion GPCRs.

The activation of adhesion GPCRs generally involves the cleavage of the GPCR autoproteolysis-inducing domain in the extracellular N terminus (*11*, *12*). This cleavage event exposes a conserved sequence known as the *stachel*, which acts as an endogenous agonist and binds to the groove in the 7-TM portion of the receptor (*13*). For example, adhesion GPCRs such as ADGRD1, ADGRG3, and ADGRG5 can be activated by their own *stachel*, which interacts with key residues in the docking pocket of transmembrane helix 5 (*10*, *14*). However, the understanding of exogenous small-molecule agonists of adhesion GPCRs remains limited. Therefore, elucidating the activation mechanisms of adhesion GPCRs by exogenous small-molecule agonists is essential for advancing our understanding of their function and developing targeted treatments for diseases in which adhesion GPCRs play key roles.

ADGRD1/GPR133 is a prominent member of the adhesion GPCR family and is implicated in various pathophysiological functions. Numerous studies have demonstrated that high ADGRD1 expression is associated with tumor progression (*15*–*20*), whereas genetic epidemiology studies have suggested that ADGRD1 single-nucleotide polymorphisms (SNPs) are associated with obesity and immune function (*20*, *21*). Compelling evidence from genome-wide association studies links ADGRD1 loci to osteoporosis and body height (*22*–*24*). These findings underscore the importance of ADGRD1 in bone diseases.

In this study, we chose ADGRD1 as a model to examine the interaction of adhesion GPCRs with exogenous agonists, with a focus on bone disease, to further explore the function of ADGRD1. We identified a small molecule, GL64 [3-(4-chlorophenyl)-2-(3-((2,4-dichlorobenzyl) oxy)phenyl)-2,3-dihydroquinazo lin-4(1*H*)-one], as a selective agonist of ADGRD1 and demonstrated that the GL64/ADGRD1 axis negatively regulates bone loss by inhibiting osteoclastogenesis via the cAMP-PKA-NFATC1 pathway. This research not only provides mechanistic insights into the activation of adhesion GPCRs by exogenous agonists but also highlights potential therapeutic approaches for osteoporosis.

---

[1]Shanghai Yangzhi Rehabilitation Hospital (Shanghai Sunshine Rehabilitation Center), Tongji University School of Medicine, Shanghai, PR. China. [2]Shanghai Key Laboratory of Regulatory Biology, Institute of Biomedical Sciences and School of Life Sciences, East China Normal University, Shanghai, PR. China. [3]Key Laboratory of Adolescent Health Assessment and Exercise Intervention of the Ministry of Education, East China Normal University, Shanghai, P. R. China. [4]Central Laboratory, The Fifth People's Hospital of Shanghai, Fudan University, Shanghai, P. R. China. [5]Advanced Medical Research Institute, Cheeloo College of Medicine, NHC Key Laboratory of Otorhinolaryngology, the Laboratory of New Cornerstone Investigator, Shandong University, Jinan, China. [6]Department of Biochemistry and Molecular Biology, School of Medicine, Shandong University, Jinan, China. [7]Leicester Cancer Research Centre, Department of Genetics and Genome Biology, University of Leicester, Leicester, UK. [8]The Mellanby Centre for Musculoskeletal Research, Division of Clinical Medicine, University of Sheffield, Sheffield, UK.
*Corresponding author. Email: jluo@tongji.edu.cn (J.L.); hyyang@bio.ecnu.edu.cn (H.Y.); yeqingsun@tongji.edu.cn (Y.S.); qszhang@bio.ecnu.edu.cn (Q.Z.)
†These authors contributed equally to this work.

RESULTS

GL64 is identified as a selective agonist of ADGRD1

First, we performed adhesion GPCR agonist screening using ADGRD1 as a model to gain mechanistic insights into the agonist activation of adhesion GPCRs (Fig. 1A). Virtual screening was used to identify potential ADGRD1 agonists from a subset of molecules in the ChemDiv and Specs databases using the three-dimensional (3D) structure of human ADGRD1 [PDB (Protein Data Bank) code: 7EPT] (*10*). Specifically, the central cavity formed by the transmembrane domain, which plays a crucial role in binding the endogenous *stachel* agonist sequence, was selected as the docking pocket.

From the top 1000 molecules based on docking scores, 79 compounds were selected for further biochemical verification using a CRE-luciferase assay (table S1). Among these small molecules, five, including GL58, GL64, GL76, GL78, and GL79, were notably more strongly activated in ADGRD1-overexpressing cells than in vector-transfected cells (tables S2 and S3). These compounds were capable of stimulating CRE-luciferase activity by more than 1.5-fold in ADGRD1-overexpressing human embryonic kidney (HEK) 293T

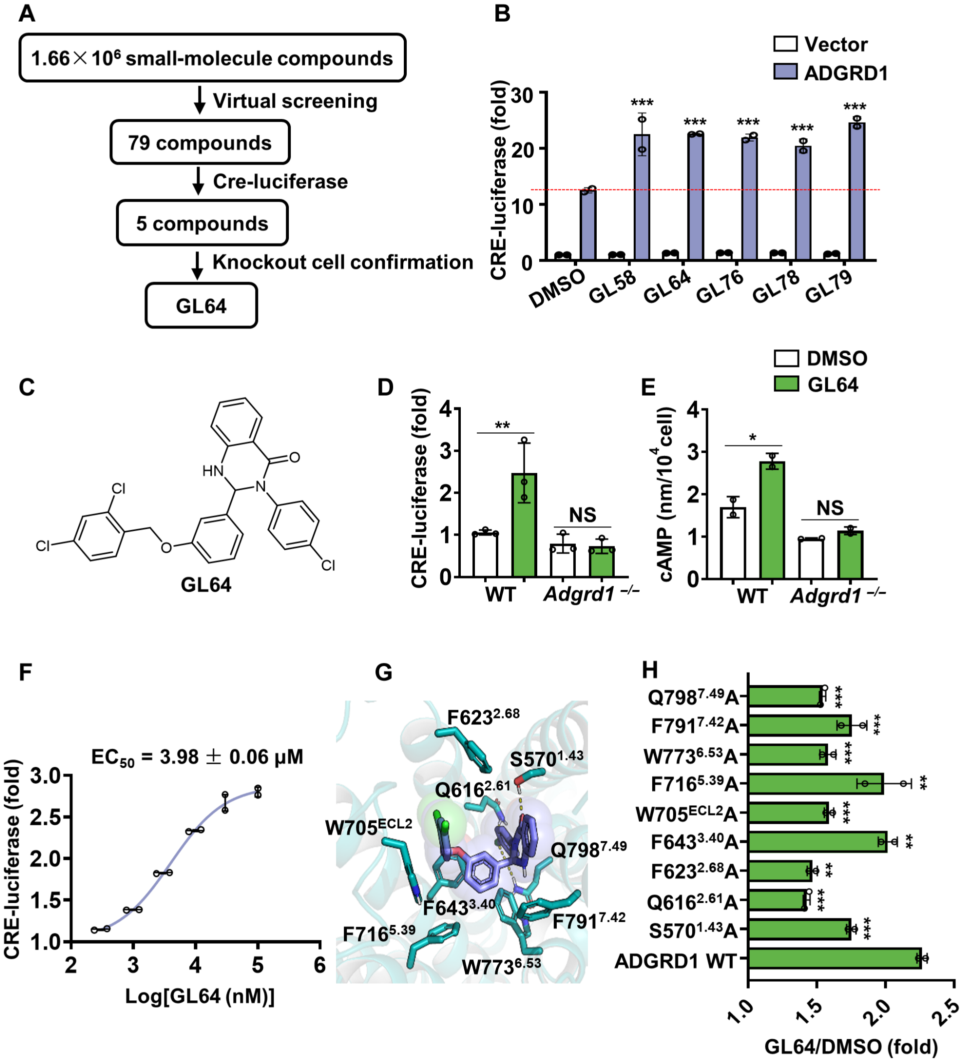

Fig. 1. GL64 was identified as a selective agonist of ADGRD1 in vitro. (**A**) Illustration of the process used to identify specific agonists of ADGRD1. (**B**) Relative CRE-luciferase expression in vector control and ADGRD1-overexpressing HEK293T cells after treatment with a series of compounds (10 μM). Each column was compared with the ADGRD1-overexpressing control column ($F_{5,12} = 12.80$, $P = 0.0002$). The data are presented as the means ± SD. ***$P < 0.001$. Two independent biological replicates were performed. (**C**) Chemical structure of GL64. (**D**) Relative CRE-luciferase expression in WT and *Adgrd1*$^{-/-}$ MEFs treated with GL64 (10 μM) ($F_{3,9} = 22.41$, $P = 0.0002$). The data are presented as the means ± SD. **$P < 0.01$; NS, not significant. Three independent biological replicates were performed. (**E**) Endogenous cAMP concentration in WT and *Adgrd1*$^{-/-}$ MEFs treated with GL64 (30 μM) ($F_{3,3} = 52.10$, $P = 0.0044$). The data are presented as the means ± SD. *$P < 0.05$. Two independent biological replicates were performed. (**F**) Concentration-response curves of ADGRD1 in response to stimulation with GL64. The data are presented as the means ± SD. The values are shown as the average of two experiments. (**G**) Detailed interaction between GL64 and ADGRD1. The GL64 molecule is shown as a slate stick, and the key residue side chains of ADGRD1 are shown as deep teal sticks. (**H**) Alanine mutagenesis scanning of putative residues in the ADGRD1 ligand binding pocket on GL64-induced cAMP inhibition in a CRE-luciferase assay ($F_{1,9} = 9.129$, $P = 0.0144$). The data are presented as the means ± SD. *$P < 0.05$, **$P < 0.01$, and ***$P < 0.001$. Two independent biological replicates were performed.

cells compared with the dimethyl sulfoxide (DMSO)–treated group but failed to stimulate CRE-luciferase activity in vector-only HEK293T cells (≤1.5-fold increase) (Fig. 1B). Further analysis of mouse embryonic fibroblasts (MEFs) revealed that GL64 was a selective agonist of ADGRD1 (Fig. 1C). GL64 increased CRE-luciferase and endogenous adenosine 3′,5′-monophosphate (cAMP) levels in wild-type (WT) MEFs but had no effect on *Adgrd1*$^{-/-}$ cells (Fig. 1, D and E). In contrast, the other molecules (GL58, GL76, GL78, and GL79) were not selective for ADGRD1 because of increased CRE-luciferase in *Adgrd1*$^{-/-}$ MEFs (fig. S1 and table S4).

The EC_{50} of GL64 was determined to be 3.98 ± 0.06 μM in a CRE-luciferase assay performed in ADGRD1-overexpressing HEK293T cells (Fig. 1F). Selectivity tests revealed that GL64 did not increase CRE-luciferase in HEK293T cells overexpressing adhesion GPCRs, such as ADGRD2, ADGRG5, ADGRG6, CELSR1, CELSR2, CELSR3, and ADGRG4 (fig. S2A and table S5). In addition, GL64 did not activate nonadhesion GPCRs, including GPR68, NPFFR1, GPR183, and GPRC5B (fig. S2B and table S5) (*25*–*28*). Together, these results demonstrated that GL64 selectively activates ADGRD1.

Structure-based compound docking analysis suggested that GL64 binds to ADGRD1 through hydrophobic interactions with nine residues (S570$^{1.43}$, Q616$^{2.61}$, F623$^{2.68}$, F643$^{3.40}$, W705^{ECL2}, F716$^{5.39}$, W773$^{6.53}$, F791$^{7.42}$, and Q798$^{7.49}$) in the binding pocket (Fig. 1G). The dihydroquinazolin group of GL64 forms a hydrogen bond with the key residue S570$^{1.43}$, and two halogen bonds were observed between the chlorobenzene group of GL64 and residues Q616$^{2.61}$ and Q798$^{7.49}$ at the bottom of the receptor binding pocket. In addition, a π-π interaction between the dichlorobenzene group of GL64 and the key receptor transmembrane domain residue W705^{ECL2} stabilizes the complex. Subsequently, alanine mutagenesis of these nine interacting residues impaired ADGRD1 activity in response to GL64 stimulation (Fig. 1H and table S6), confirming their roles in GL64 binding.

Given that GL64 binds to the pocket that normally accommodates the *stachel* sequence, we next investigated whether mutations of key *stachel* residues, which interact with residues of the orthosteric binding pocket of the 7-TM portion of ADGRD1 (*10*), affect receptor activation by GL64. Alanine mutations at residues I549, L550, and V553 enhanced ADGRD1 activation by GL64 (fig. S3A and table S6). The EC_{50} of GL64 in *stachel* peptide–treated ADGRD1-overexpressing cells was 16.89 ± 2.96 μM (fig. S3B and table S7), which was greater than that in untreated cells (3.98 ± 0.06 μM). Collectively, these results suggest that GL64 may compete with the endogenous *stachel* sequence as an orthosteric agonist of ADGRD1. In addition, we found that the fold change following the expression of an ADGRD1 WT plasmid stimulated with GL64 was greater than that following the expression of a noncleavable ADGRD1 mutant plasmid (fig. S3C), suggesting that receptor cleavage may affect the activation by GL64.

To further investigate the binding and activation of ADGRD1 by GL64, we conducted molecular dynamics (MD) simulations. Two simulation models of the ADGRD1 structure, with or without GL64, were subjected to three independent 1-μs MD simulations using GROMACS software. The results showed that GL64 exhibited high stability throughout the course of the simulations, as indicated by low root mean square deviation (RMSD) values (Fig. 2A). In addition, the nine residues of ADGRD1 identified to interact with GL64 in our docking model consistently maintained contact with GL64 during the simulations (Fig. 2B). These findings indicate that GL64 plays a vital role in stabilizing the active conformation of ADGRD1. Notably, the distance between W773$^{6.53}$ and Q798$^{7.49}$ remained stable upon stimulation in the presence of GL64 (Fig. 2C), whereas it varied and increased in the absence of GL64 (Fig. 2D). Moreover, the interaction between W773$^{6.53}$ and Q798$^{7.49}$ was verified by the cryo–electron microscopy (cryo-EM) structure of the *stachel*-ADGRD1 complex (Fig. 2E) (*10*). These findings demonstrate that GL64, similar to the endogenous agonist *stachel*, stabilizes the active conformation of ADGRD1 by preserving interactions between W773$^{6.53}$ and Q798$^{7.49}$, thereby triggering an agonistic effect.

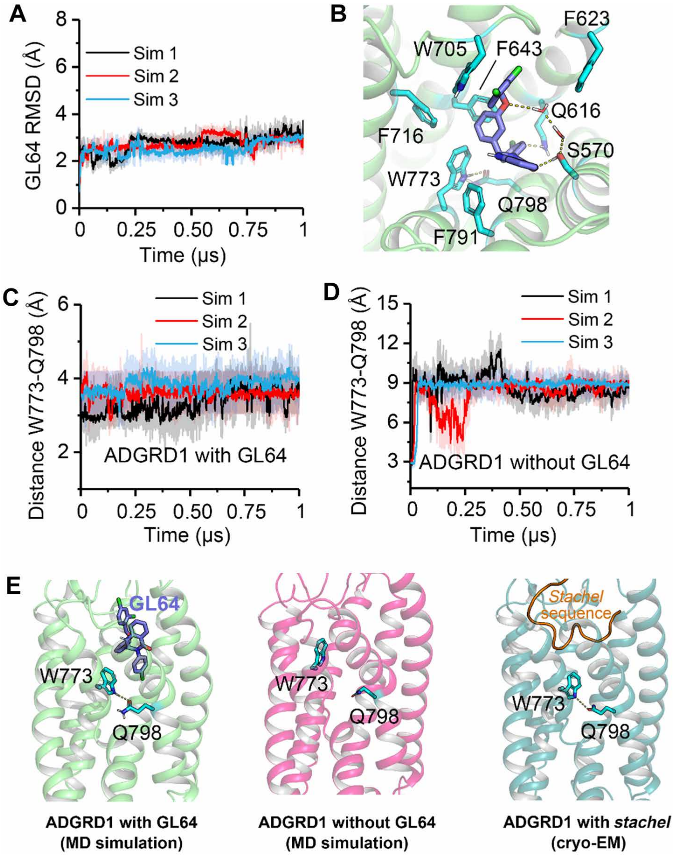

Fig. 2. Potential activation mechanisms of the GL64 molecule in ADGRD1 from MD simulations. (**A**) RMSD of the small molecule GL64 during three independent 1-μs MD simulations for the GL64-ADGRD1 complex. Sim, simulation. (**B**) Structural representation of the interaction of GL64 with ADGRD1 according to MD simulations. The values were calculated on the basis of the final snapshot of the 1-μs MD simulation. GL64 is represented by purple sticks, and key residues are shown as blue sticks. (**C**) Time evolution of the distance changes between W773$^{6.53}$ and Q798$^{7.49}$ during three independent 1-μs MD simulations in ADGRD1 with GL64. (**D**) Time evolution of the distance changes between W773$^{6.53}$ and Q798$^{7.49}$ during three independent 1-μs MD simulations in ADGRD1 without GL64. (**E**) Detailed interactions between W773$^{6.53}$ and Q798$^{7.49}$ in the ADGRD1-GL64 complex (the final MD snapshot), apo state ADGRD1 (the final MD snapshot), and ADGRD1 with the *stachel* segment (cryo-EM structure).

The bone phenotype is altered in adult *Adgrd1*-deficient mice

We next investigated the therapeutic efficacy of GL64 in vivo through the newly identified function of ADGRD1. Because SNPs of ADGRD1 are associated with short stature and osteoporosis in humans, we examined the roles of ADGRD1 in the mouse skeletal system. First, we validated the establishment of an *Adgrd1* knockout mouse line by confirming the lack of *Adgrd1* mRNA and protein expression (fig. S4, A to F). We found that, compared with WT littermate controls, the knockout of *Adgrd1* had little, if any, effect on body length during the embryonic (14.5 and 18.5 days), prenatal (0 days), and postnatal (8 weeks) stages (Fig. 3, A to E). Consistently, skeleton alcian blue and alizarin red staining revealed that *Adgrd1* knockout also had little effect on bone development (Fig. 3A).

However, bone mass analysis revealed nearly 50% decreases in trabecular bone volume (BV/TV), bone mineral density (BMD), and the number of trabeculae (TB. N), whereas trabecular spacing (TB. SP) was greater in both male and female *Adgrd1*$^{-/-}$ mice than in WT littermates, regardless of age (Fig. 3, F and G), or in 4-week-old mice (fig. S5, A and B). Cortical bone parameters were not affected in *Adgrd1*$^{-/-}$ mice compared to littermate WT mice (fig. S6, A and B). Similar results were observed for spine bone mass in bone histomorphometry analysis, which revealed decreases in the trabecular BV/TV, TB. N, and trabecular thickness (TB.TH) and an increase in the TB. SP in *Adgrd1*$^{-/-}$ mice (Fig. 3, H and I).

Osteoclastogenesis is promoted in *Adgrd1*-deficient mice

To investigate how ADGRD1 regulates the balance between bone resorption and bone formation and subsequently modulates bone mass, we analyzed the activity levels of bone-resorbing cells (osteoclasts) and bone-forming cells (osteoblasts) in vivo. Our data revealed that the expression of tartrate-resistant acid phosphatase (TRAP), a marker of mature osteoclasts, was greater in the femurs of *Adgrd1*$^{-/-}$ mice than in those of littermate WT mice (Fig. 4, A and B). TRAP enzyme activity in femurs was elevated following *Adgrd1* knockout, along with increases in the number of osteoclasts (N. OC/B) and erosion surface area [eroded surface/bone surface (ES/BS)] in *Adgrd1*$^{-/-}$ mice (Fig. 4, C and D). Similarly, TRAP enzyme activity was increased in the calvarias of *Adgrd1*$^{-/-}$ mice (Fig. 4, E to H). These results demonstrate that *Adgrd1* knockout promotes osteoclastogenesis.

We then examined bone formation in WT and *Adgrd1*$^{-/-}$ mice. Goldner's staining revealed increases in the number of osteoblasts and the size of the osteoid surface in *Adgrd1*$^{-/-}$ mice (fig. S7, A and B). In addition, a calcein double-labeling assay revealed that the bone formation rate and mineral apposition rate were greater in *Adgrd1*$^{-/-}$ mice than in WT littermate controls (fig. S7, C and D). These results indicate that *Adgrd1* knockout can promote both bone resorption and bone formation. However, the decrease in bone mass observed in *Adgrd1*$^{-/-}$ mice suggests that ADGRD1 primarily regulates bone mass by negatively modulating osteoclastogenesis.

Specific knockout of *Adgrd1* in osteoclasts decreases bone mass by promoting osteoclastogenesis in vivo

To verify the function of ADGRD1 in osteoclasts, we generated *Adgrd1* osteoclast-conditional knockout mice (*Adgrd1*^{Lysm}) by crossing lysozyme M promoter–driven Cre (Lysm-Cre) mice (*7*, *29*–*32*) with *Adgrd1*$^{flox/flox}$ mice, and the lack of mRNA and protein expression of *Adgrd1* in osteoclasts was confirmed (fig. S8, A to E). Compared with those in littermate control mice, *Adgrd1* knockout in osteoclasts led to decreases in trabecular BV/TV, BMD, and TB. N (Fig. 5, A and B). However, cortical bone parameters were not affected (fig. S9, A and B). Immunostaining was then performed to further investigate osteoclastogenesis in *Adgrd1*^{Lysm} mice and revealed enhanced TRAP expression in *Adgrd1*^{Lysm} mice compared with control mice (Fig. 5, C and D). TRAP enzyme activity in the femur increased, as did N. OC/B and ES/BS (Fig. 5, E and F). Similarly, TRAP enzyme activity in the calvarias was increased in *Adgrd1*^{Lysm} mice (Fig. 5, G to J). These results demonstrate that knocking out *Adgrd1* leads to osteoporosis by promoting osteoclastogenesis.

Depletion of *Adgrd1* promotes osteoclast differentiation and bone resorption in vitro

To further investigate the role of ADGRD1 in osteoclast maturation and bone resorption, we first performed single-cell sequencing analysis of the expression of *Adgrd1* in bone tissue data from the Gene Expression Omnibus database, which revealed that *Adgrd1* is highly expressed in osteoclasts (fig. S10, A and B). Then, we isolated bone marrow monocyte/macrophage (BMM) cells from 8-week-old male WT and *Adgrd1*$^{-/-}$ mice, and osteoclast differentiation was induced by stimulation with macrophage colony-stimulating factor (M-CSF; 10 ng/ml) and receptor activator of nuclear factor κB ligand (RANKL; 100 ng/ml) (*30*). During differentiation, *Adgrd1* expression also increased (fig. S11A). Moreover, both male and female *Adgrd1*$^{-/-}$ BMMs displayed increased osteoclast differentiation, as evidenced by greater osteoclast numbers and areas (fig. S11, B and C). In addition, male *Adgrd1*$^{-/-}$ BMMs exhibited accelerated differentiation into mature osteoclasts (Fig. 6, A and B). *Adgrd1* knockout also increased BMM responsiveness to suboptimal RANKL dosages (Fig. 6, C and D). Using real-time polymerase chain reaction (PCR), we next detected elevated levels of osteoclast differentiation markers, including *Nfatc1*, *Dc-stamp*, and *Acp5*, in male *Adgrd1*-deficient BMMs during their differentiation into mature osteoclasts (fig. S11D). A resorption pit assay further demonstrated that male *Adgrd1*$^{-/-}$ osteoclasts formed larger and deeper pits than WT osteoclasts did (Fig. 6, E to G).

Consistent with the findings from the genetic depletion studies, the activation of ADGRD1 with GL64 (10 μM) inhibited the differentiation of male WT BMMs into mature osteoclasts but had no effect on *Adgrd1*$^{-/-}$ cells (Fig. 6, H and I). GL64 treatment downregulated the expression levels of osteoclastogenesis-related genes, including *Dc-stamp*, *Acp5*, and *Nfatc1*, during male mouse osteoclast maturation (fig. S11E). These findings demonstrate that GL64/ADGRD1 negatively regulates osteoclast maturation and bone resorption, further underscoring the importance of this pathway in maintaining bone homeostasis.

GL64/ADGRD1 regulates osteoclast differentiation via the cAMP-PKA-NFATC1 signaling pathway

We next investigated the molecular mechanism through which ADGRD1 and GL64 regulate osteoclast differentiation. Our data revealed that endogenous cAMP levels increased in male BMMs treated with GL64 or in a mouse macrophage line (RAW264.7) following *Adgrd1* overexpression under RANKL stimulation (Fig. 7, A and B), and RAW264.7 cells were selected from among monoclonal cells for differentiation into mature osteoclasts induced by RANKL (*30*). We also found that H89, a cAMP-dependent protein kinase (PKA) inhibitor, rescued the inhibition of osteoclast differentiation induced by GL64 treatment in male BMMs (Fig. 7, C and D). Conversely, forskolin, an adenylate cyclase agonist, suppressed excessive osteoclastogenesis in *Adgrd1*$^{-/-}$ cells (fig. S12, A and B). Many receptors, including but not limited to ADGRE5 and ADGRF1, are expressed in osteoclasts and can stimulate cAMP production (*33*–*35*). Therefore,

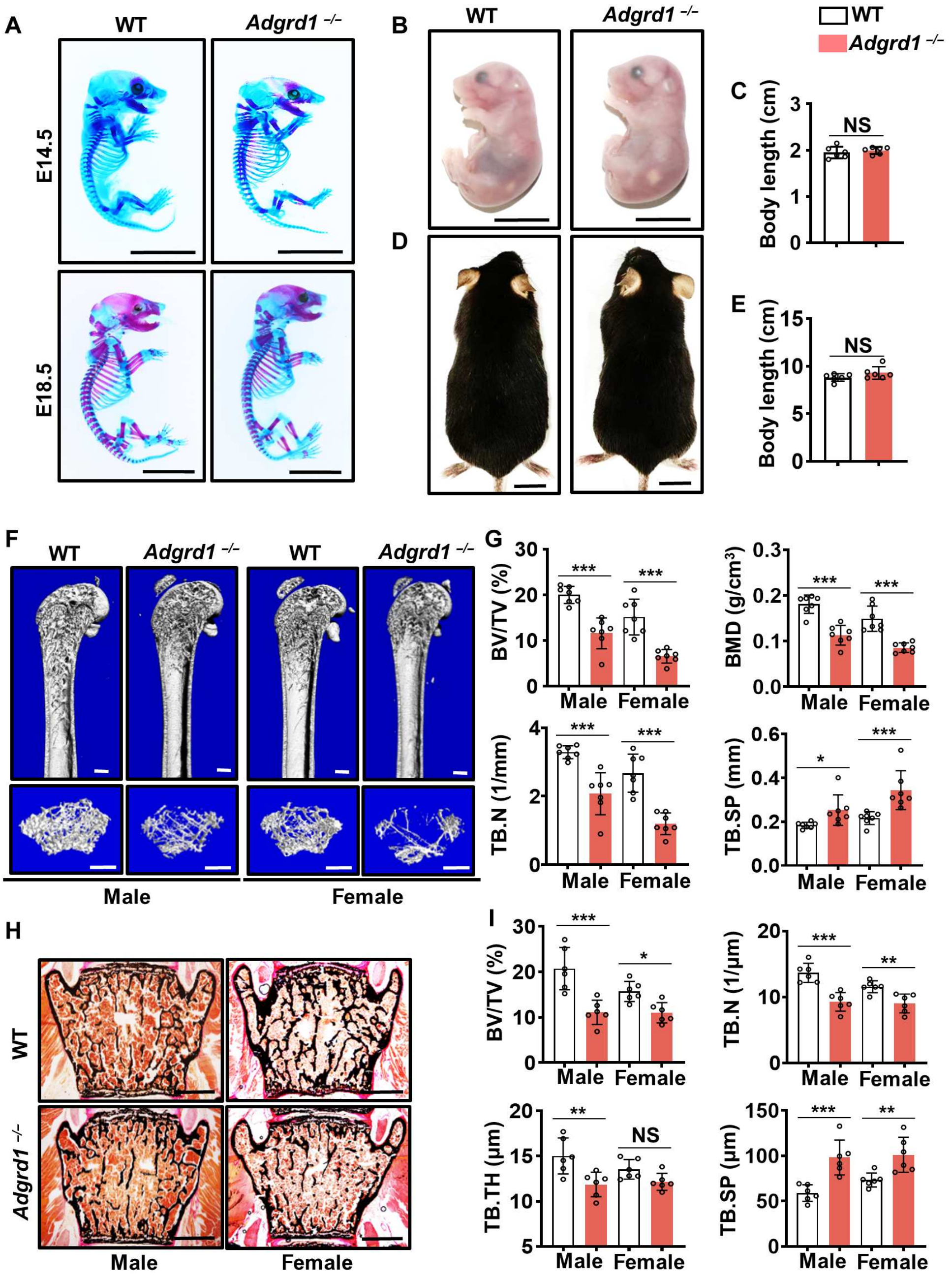

Fig. 3. Bone phenotype of *Adgrd1*-deficient mice. (**A**) Representative alcian blue and alizarin red staining images of whole skeletal preparations from WT and *Adgrd1*$^{-/-}$ mice at embryonic day 14.5 (E14.5) and embryonic day 18.5 (E18.5). Scale bars, 1 cm. (**B**) Representative images of WT and *Adgrd1*$^{-/-}$ mice at P0. Scale bars, 1 cm. (**C**) The body length (nose-to-tail) was measured and compared between WT and *Adgrd1*$^{-/-}$ mice at P0. The data are presented as the means ± SD. $n = 6$. (**D**) Representative images of WT and *Adgrd1*$^{-/-}$ mice at postnatal week 8. Scale bars, 1 cm. (**E**) The body length (nose-to-tail) was measured and compared between WT and *Adgrd1*$^{-/-}$ mice at postnatal week 8. The data are presented as the means ± SD. $n = 6$. (**F**) Representative micro-CT images of the femurs of 8-week-old WT and *Adgrd1*$^{-/-}$ mice showing the distal femur (top; scale bars, 500 μm) and trabeculae (bottom; scale bars, 200 μm). (**G**) Quantitative micro-CT analysis of the trabecular bone parameters of the femurs shown in (F) (BV/TV: $F_{3,18} = 31.04$, $P < 0.0001$; BMD: $F_{3,18} = 28.83$, $P < 0.0001$; TB. N: $F_{3,18} = 28.68$, $P < 0.0001$; TB. SP: $F_{3,18} = 16.12$, $P < 0.0001$). The data are presented as the means ± SD. $^*P < 0.05$ and $^{***}P < 0.001$. $n = 7$. (**H**) Representative images of von Kossa staining of vertebral sections from 8-week-old WT and *Adgrd1*$^{-/-}$ mice. Scale bars, 500 μm. (**I**) Trabecular bone parameters were compared between the WT and *Adgrd1*$^{-/-}$ mice shown in (H) (BV/TV: $F_{3,15} = 16.59$, $P < 0.0001$); TB. N: $F_{3,15} = 25.96$, $P < 0.0001$; TB.TH: $F_{3,15} = 7.058$, $P = 0.0035$; TB. SP: $F_{3,15} = 14.92$, $P < 0.0001$). The data are presented as the means ± SD. $^*P < 0.05$, $^{**}P < 0.01$, and $^{***}P < 0.001$. $n = 6$.

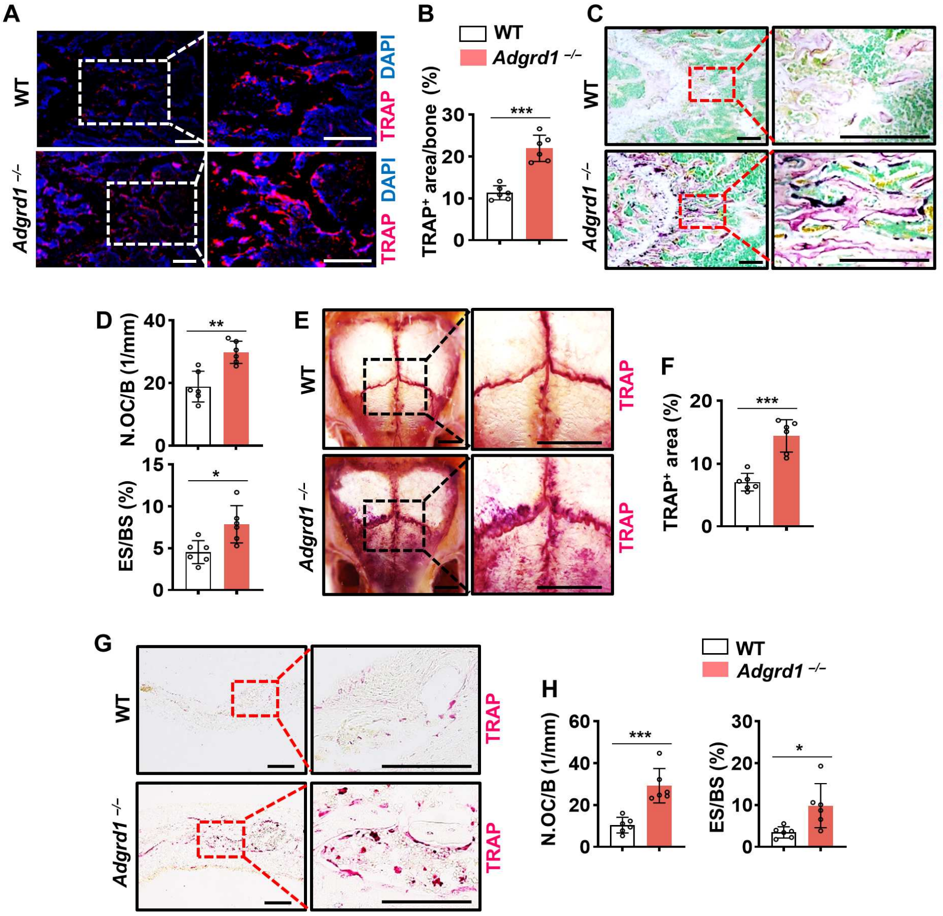

Fig. 4. Osteoclastogenesis is promoted in *Adgrd1*-deficient mice. (**A**) Representative immunofluorescence images of TRAP-stained femurs from 8-week-old male WT and *Adgrd1*$^{-/-}$ mice. Scale bars, 100 μm. (**B**) Percentage of TRAP-positive areas in the bone samples shown in (A). The data are presented as the means ± SD. ***$P < 0.001$; $n = 6$. (**C**) Representative TRAP staining images of femur osteoclasts from 8-week-old male WT and *Adgrd1*$^{-/-}$ mice. Scale bars, 100 μm. (**D**) Quantification of femur osteoclasts from the 8-week-old WT and *Adgrd1*$^{-/-}$ mice shown in (C). The data are presented as the means ± SD. *$P < 0.05$ and **$P < 0.01$; $n = 6$. (**E**) Representative image of TRAP staining of the calvarias of 8-week-old male WT and *Adgrd1*$^{-/-}$ mice. Scale bars, 1 mm. (**F**) Percentage of TRAP-positive areas in the calvarias of the samples shown in (E). The data are presented as the means ± SD. ***$P < 0.001$; $n = 6$. (**G**) Representative TRAP staining images of calvarias from 8-week-old male WT and *Adgrd1*$^{-/-}$ mice. Scale bars, 100 μm. (**H**) Parameters of calvarial osteoclastogenesis in 8-week-old WT and *Adgrd1*$^{-/-}$ mice. The data are presented as the means ± SD. *$P < 0.05$ and ***$P < 0.001$; $n = 6$.

Adgrd1 knockout does not result in the complete absence of cAMP, and phosphodiesterases can still degrade residual cAMP. To further investigate this, we used 3-isobutyl-1-methylxanthine (IBMX) to inhibit phosphodiesterase activity and increase basal cAMP levels in WT and *Adgrd1*$^{-/-}$ osteoclasts. The results showed that IBMX suppressed excessive osteoclastogenesis following *Adgrd1* knockout (Fig. 7, E and F). These findings support the hypothesis that ADGRD1 regulates osteoclast differentiation through the cAMP-PKA pathway. Furthermore, nuclear factor of activated T cells 1 (NFATC1), a key transcription factor required for osteoclast maturation, can be phosphorylated by PKA, which inhibits its nuclear translocation and activity (*36*–*39*). We found that GL64 treatment or *Adgrd1* overexpression reduced NFATC1 nuclear localization, whereas H89 treatment reversed the GL64-induced inhibition of NFATC1 nuclear translocation (Fig. 7, G and H, and fig. S13, A and B). In contrast, compared with WT BMMs isolated from male mice, *Adgrd1* knockout promoted NFATC1 expression and nuclear localization after 2 days of RANKL stimulation. Treating *Adgrd1* knockout cells with forskolin blocked NFATC1 expression and nuclear localization, restoring NFATC1 levels comparable to those in WT cells (fig. S13, C and D). These results demonstrate that GL64/ADGRD1 regulates NFATC1 nuclear localization via the cAMP-PKA pathway, providing a mechanistic basis for its role in osteoclast differentiation.

GL64 rescues ovariectomy-induced bone loss and osteoclast hyperactivity in vivo

To examine whether GL64 functions in vivo, we first evaluated GL64 pharmacokinetics in male mouse plasma. A 30 mg/kg intraperitoneal injection of GL64 resulted in a maximum plasma concentration ($C_{\max}$) of 26,563 ng/ml at 1 hour, with an elimination half-life ($t_{1/2}$) of 6.27 hours (fig. S14A). In addition, we found that the intraperitoneal injection of GL64 allows it to reach the BMM niche within the bone marrow. The same 30 mg/kg intraperitoneal injection dose produced a maximum bone marrow concentration of 3378 ng/ml at 1 hour, which remained at a high concentration of 1320 ng/ml after 4 hours (fig. S14B). We then evaluated the therapeutic potential

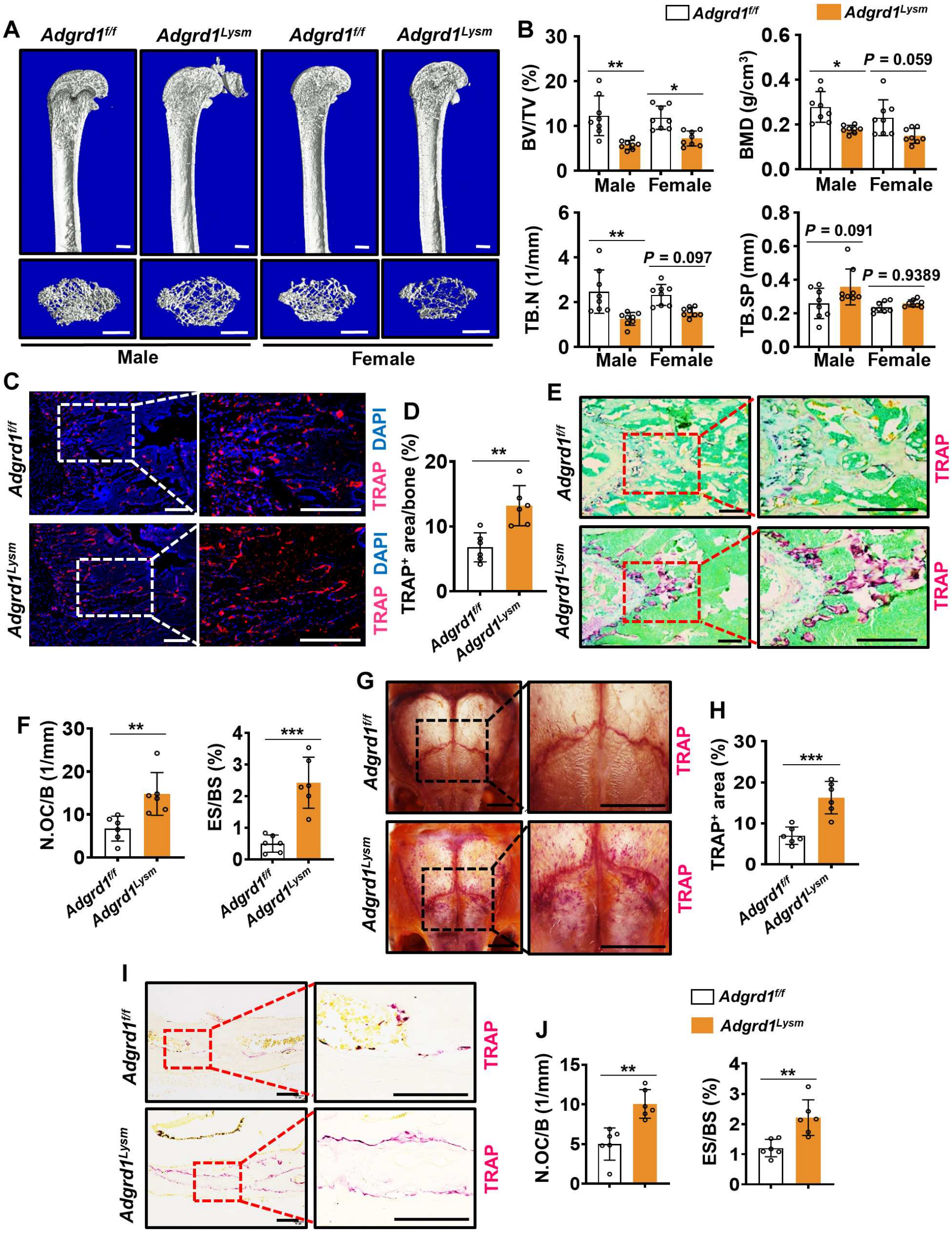

Fig. 5. Knocking out *Adgrd1* in osteoclasts decreases bone mass by promoting osteoclastogenesis. (**A**) Representative micro-CT images of the distal (top; scale bars, 500 μm) and trabecular (bottom; scale bars, 200 μm) femurs of 8-week-old *Adgrd1$^{f/f}$ and Adgrd1^{Lysm}* mice. (**B**) Quantitative micro-CT analysis of trabecular bone parameters in the femurs of 8-week-old *Adgrd1$^{f/f}$* and *Adgrd1^{Lysm}* mice (BV/TV: $F_{3,21} = 9.590$, $P = 0.0003$; BMD: $F_{3,21} = 7.283$, $P = 0.0016$; TB. N: $F_{3,21} = 7.082$, $P = 0.0018$). The data are presented as the means ± SD. $*P < 0.05$ and $**P < 0.01$. $n = 8$. (**C**) Representative images of TRAP-stained femurs from 8-week-old male *Adgrd1$^{f/f}$* and *Adgrd1^{Lysm}* mice. Scale bars, 100 μm. (**D**) Percentage of TRAP-positive areas in the bone samples shown in (C). The data are presented as the means ± SD. $**P < 0.01$; $n = 6$. (**E**) Representative TRAP-stained images of femoral osteoclasts from 8-week-old male *Adgrd1$^{f/f}$* and *Adgrd1^{Lyzm}* mice. Scale bars, 100 μm. (**F**) Quantification of parameters in the 8-week-old male *Adgrd1$^{f/f}$* and *Adgrd1^{Lyzm}* mice shown in (E). The data are presented as the means ± SD. $**P < 0.01$ and $***P < 0.001$; $n = 6$. (**G**) Representative TRAP staining of calvarias from 8-week-old male *Adgrd1$^{f/f}$* and *Adgrd1^{Lysm}* mice. Scale bars, 1 mm. (**H**) Percentage of TRAP-positive areas in calvarias shown in (G). The data are presented as the means ± SD. $***P < 0.001$; $n = 6$. (**I**) Representative TRAP staining images of calvarias from 8-week-old male *Adgrd1$^{f/f}$* and *Adgrd1^{Lysm}* mice. Scale bars, 100 μm. (**J**) Parameters of osteoclastogenesis in the calvarias of 8-week-old male *Adgrd1$^{f/f}$* and *Adgrd1^{Lysm}* mice. The data are presented as the means ± SD. $**P < 0.01$; $n = 6$.

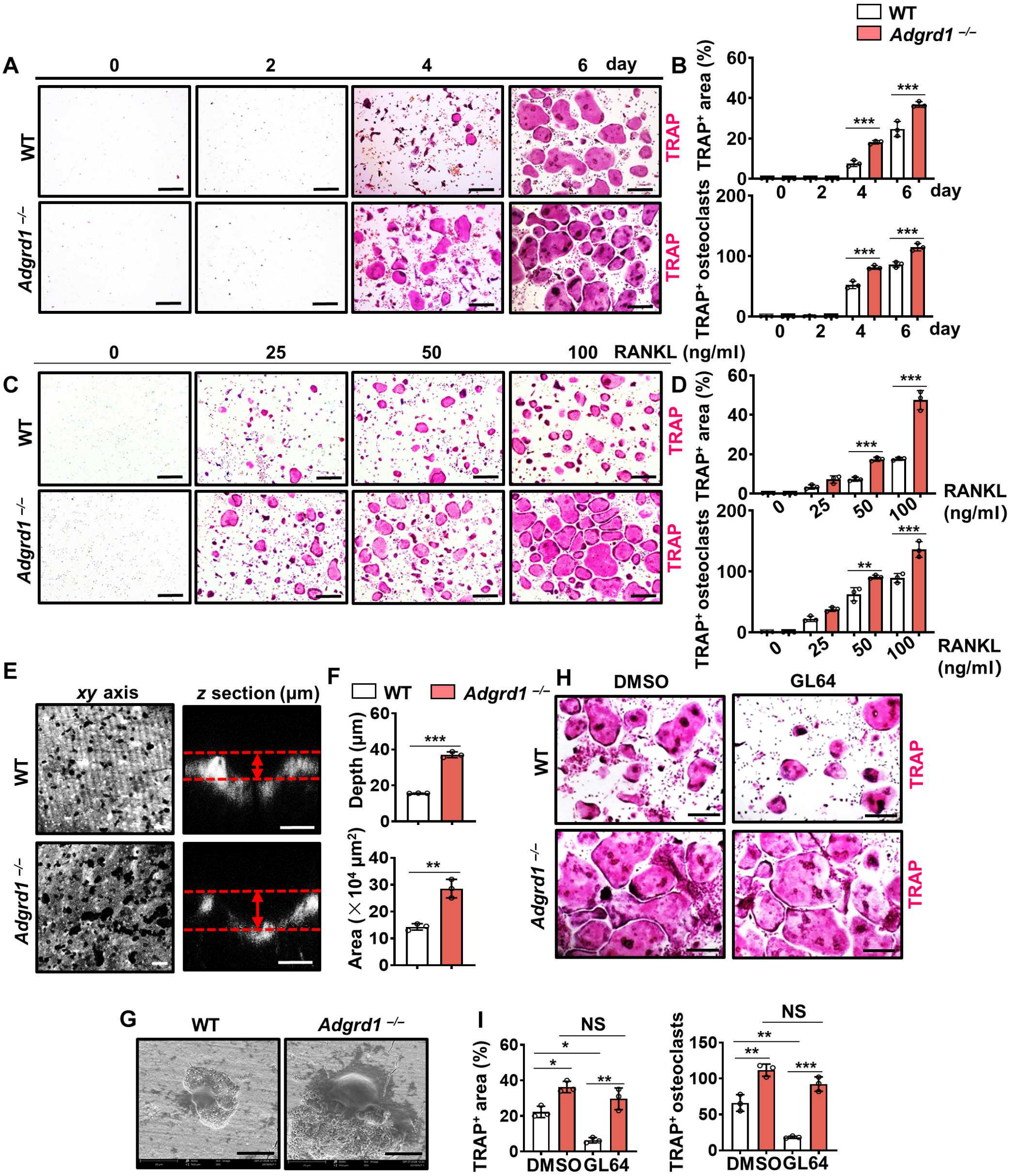

Fig. 6. *Adgrd1* knockout in BMM cells promotes osteoclast differentiation and bone resorption. (**A**) Representative TRAP staining images of cells cultured with M-CSF and RANKL for 2, 4, or 6 days isolated from WT and *Adgrd1*$^{-/-}$ male mice. Scale bars, 100 μm. (**B**) Quantification of the osteoclast area and number of the cells shown in (A) (area: $F_{7,14} = 227.6$, $P < 0.0001$; number: $F_{7,14} = 696.8$, $P < 0.0001$). The data are presented as the means ± SD. $***P < 0.001$. Three independent biological replicates were performed. (**C**) Representative TRAP staining images of WT and *Adgrd1*$^{-/-}$ BMMs cultured with M-CSF (10 ng/ml) and varying RANKL concentrations. Scale bars, 100 μm. (**D**) Quantification of osteoclast area and number from the samples shown in (C) (area: $F_{7,14} = 170.0$, $P < 0.0001$; number: $F_{7,14} = 130.6$, $P < 0.0001$). The data are presented as the means ± SD. $**P < 0.01$ and $***P < 0.001$. Three independent biological replicates were performed. (**E**) Representative confocal microscopy images of hydroxyapatite resorption by osteoclasts derived from WT and *Adgrd1*$^{-/-}$ male mice. Scale bars, 10 μm. (**F**) Quantification of bone resorption area and depth in the samples shown in (E). The data are presented as the means ± SD. $**P < 0.01$ and $***P < 0.001$. Three independent biological replicates were performed. (**G**) Representative SEM images of hydroxyapatite resorption by osteoclasts isolated from WT and *Adgrd1*$^{-/-}$ male mice. Scale bars, 20 μm. (**H**) Representative TRAP staining images of WT and *Adgrd1*$^{-/-}$ BMMs treated with RANKL (100 ng/ml) or GL64 (10 μM) for 6 days. Scale bars, 50 μm. (**I**) Quantification of the osteoclast area and number of the cells shown in (H) (area: $F_{3,6} = 26.13$, $P = 0.0008$; number: $F_{3,6} = 50.43$, $P = 0.0001$). The data are presented as the means ± SD. $*P < 0.05$, $**P < 0.01$, and $***P < 0.001$. Three independent biological replicates were performed.

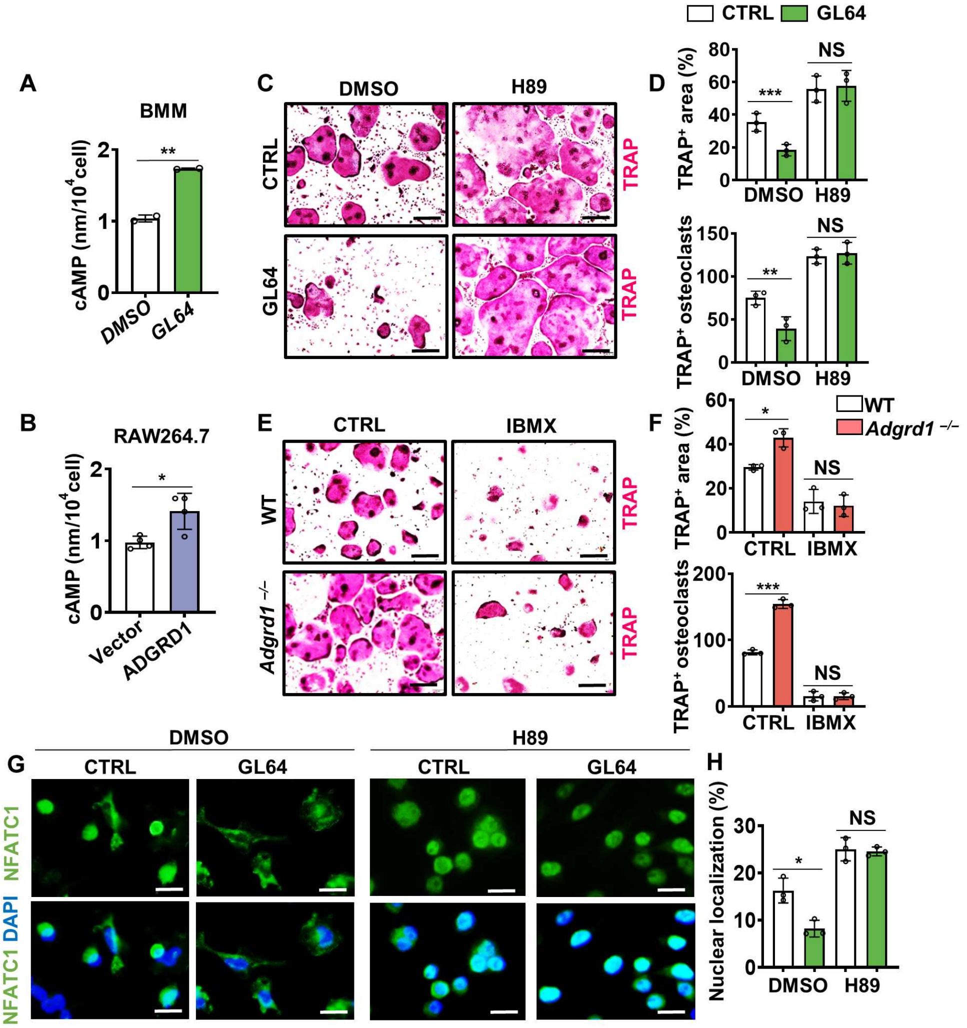

Fig. 7. GL64/ADGRD1 regulates osteoclast maturation through the cAMP-PKA-NFATC1 pathway. (**A**) Intracellular cAMP levels in WT BMM cells after induction with RANKL (100 ng/ml), DMSO, or GL64 (30 μM). The data are presented as the means ± SD. $^{**}P < 0.01$. Two independent biological replicates were performed. (**B**) Intracellular cAMP levels in vector- and *ADGRD1*-overexpressing RAW264.7 cells. The data are presented as the means ± SD. $^{*}P < 0.05$. Four independent biological replicates were performed. (**C**) Representative images of TRAP staining of BMMs treated with DMSO, GL64 (10 μM), or H89 (1 μM) and stimulated with RANKL (100 ng/ml) for 6 days. Scale bars, 50 μm. (**D**) Quantification of osteoclast area and number shown in (C) (area: $F_{3,6} = 45.34$, $P = 0.0002$; number: $F_{3,6} = 69.20$, $P < 0.0001$). The data are presented as the means ± SD. $^{**}P < 0.01$ and $^{***}P < 0.001$. Three independent biological replicates were performed. (**E**) Representative TRAP staining images of WT and $Adgrd1^{-/-}$ BMMs treated with RANKL (100 ng/ml) or IBMX (50 μM) for 6 days. Scale bars, 50 μm. (**F**) Quantification of the osteoclast area (top) and number (bottom) of the cells shown in (E) (area: $F_{3,6} = 30.08$, $P = 0.0005$; number: $F_{3,6} = 291.4$, $P < 0.0001$). The data are presented as the means ± SD. $^{*}P < 0.05$ and $^{***}P < 0.001$. Three independent biological replicates were performed. (**G**) Representative images of NFATC1 nuclear translocation in BMM cells treated with DMSO, GL64 (10 μM), or H89 (1 μM) and stimulated with RANKL (100 ng/ml) for 2 days. Scale bars, 50 μm. (**H**) Percentage of NFATC1 nuclear localization in the samples shown in (G) ($F_{3,6} = 34.52$, $P = 0.0004$). Data are presented as the means ± SD. $^{*}P < 0.05$. Three independent biological replicates were performed.

of GL64 using ovariectomized mice as a model for postmenopausal osteoporosis (Fig. 8A). Compared with no treatment, GL64 treatment markedly rescued ovariectomy (OVX)–induced bone loss, as evidenced by increased BMD, BV/TV, and TB. N (Fig. 8, B and C). GL64 also inhibited OVX-induced TRAP expression and enzyme hyperactivity in femurs. The osteoclast number and surface erosion were lower in the GL64-treated group than in the OVX group (Fig. 8, D to G). Similarly, GL64 markedly suppressed TRAP enzyme activity in the calvarias (Fig. 8, H and I). These findings demonstrate that GL64 can rescue OVX-induced osteoclast hyperactivity and bone loss, highlighting its potential as a pharmaceutical agent for treating hyperactive osteoclast–related diseases, such as osteoporosis.

DISCUSSION

In this study, we identified GL64 as a selective agonist of ADGRD1, revealing a previously unidentified function of ADGRD1 in the regulation of bone disease. GL64 effectively suppressed osteoclastogenesis and prevented bone loss both in vivo and in vitro. We demonstrated that the cAMP-PKA-NFATC1 pathway serves as a critical downstream signaling mechanism in the GL64/ADGRD1–mediated regulation of osteoclast maturation. Thus, our study not only establishes GL64 as a viable probe molecule for the functional exploration of ADGRD1 but also provides mechanistic insights into the activation of adhesion GPCRs by exogenous agonists.

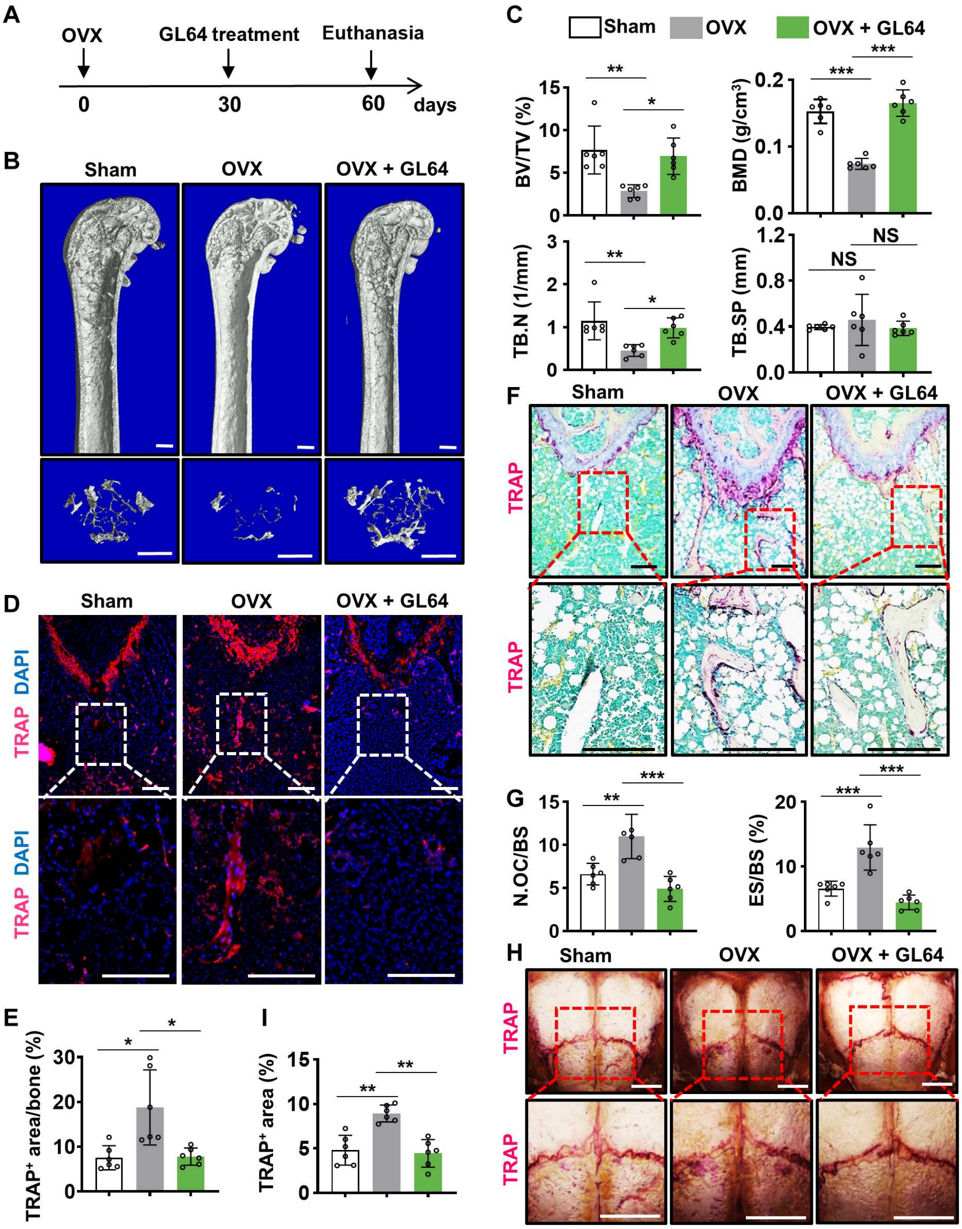

Fig. 8. GL64 rescues OVX-induced bone loss and osteoclast hyperactivity. (**A**) Schematic diagram showing the experimental design for GL64 treatment in OVX-induced osteoporosis mice. (**B**) Representative micro-CT images of the distal femur (top; scale bars, 500 μm) and trabecula (bottom; scale bars, 200 μm) after 1 month of GL64 treatment in the OVX-induced mouse model. (**C**) Quantitative micro-CT analysis of trabecular bone parameters from the samples shown in (B) (BV/TV: $F_{2,10} = 9.656$, $P = 0.0046$; BMD: $F_{2,10} = 44.34$, $P < 0.0001$; TB. N: $F_{2,10} = 10.02$, $P = 0.0041$). The data are presented as the means ± SD. $^{*}P < 0.05$, $^{**}P < 0.01$, and $^{***}P < 0.001$. $n = 6$. (**D**) Representative immunofluorescence images of TRAP-stained femurs from OVX-induced mice treated with GL64 for 1 month. Scale bars, 100 μm. (**E**) Percentage of TRAP-positive areas in the bone samples shown in (D). The data are presented as the means ± SD ($F_{2,10} = 7.906$, $P = 0.0087$). $^{*}P < 0.05$. $n = 6$. (**F**) Representative TRAP staining images of femur osteoclasts in the OVX-induced mouse model after 1 month of GL64 treatment. Scale bars, 100 μm. (**G**) Parameters of the femur osteoclasts shown in (F) (N. OC/B: $F_{2,10} = 27.49$, $P < 0.0001$; ES/BS: $F_{2,10} = 30.28$, $P < 0.0001$). The data are presented as the means ± SD. $^{**}P < 0.01$ and $^{***}P < 0.001$. $n = 6$. (**H**) Representative TRAP staining images of calvarias from OVX-induced mice after 1 month of GL64 treatment. Scale bars, 1 mm. (**I**) Percentage of TRAP-positive areas in calvarias from the samples shown in (H) ($F_{2,10} = 16.30$, $P = 0.0007$). The data are presented as the means ± SD. $^{**}P < 0.01$. $n = 6$.

The discovery of exogenous small molecules that target adhesion GPCRs has been challenging because of the structural complexity and intricate modulation mechanisms of this GPCR family. However, recent advances, including the solution of the cryo-EM structures of ADGRG3, ADGRG5, and ADGRD1 (*10*, *14*), have provided a foundation for the design of adhesion GPCR-targeting molecules. In this study, a small molecule, GL64, was designed on the basis of the activation conformation of ADGRD1, and its mechanism of action was explored. MD simulations revealed that GL64 stabilizes the agonistic conformation of ADGRD1 by maintaining key interactions with residues W773$^{6.53}$ and Q798$^{7.49}$. Both residues W773$^{6.53}$ and Q798$^{7.49}$ interact with the *stachel* and are conserved in several adhesion GPCRs, such as ADGRG5 (*10*). Therefore, the activation mechanisms we delineated for ADGRD1 may be generalizable across the adhesion GPCR family, potentially facilitating the discovery of agonists for other receptors in this class.

Osteoporosis is a prevalent age-related disease associated with morbidity worldwide (*40*–*42*). Safer and more effective treatments for osteoporosis are urgently needed. Our study demonstrated that *Adgrd1* knockout decreased bone mass, whereas administration of the ADGRD1 agonist GL64 effectively counteracted OVX-induced bone loss and osteoclast hyperactivity. These findings indicate that ADGRD1 is a promising drug target for osteoclast hyperactivity–related diseases, such as osteoporosis. Although our in silico screening and validation were performed using human ADGRD1, the protein sequence of mouse Adgrd1 and human ADGRD1 shares 86.09% homology, including a conserved *stachel* domain and GL64 binding sites (fig. S15). This conservation supports the potential translatability of GL64 to human clinical applications.

Despite these promising findings, there are limitations in the present study that warrant further investigation. For example, although our biochemical data demonstrated that GL64 can stimulate the cAMP pathway via ADGRD1, crystallographic analysis could provide more definitive evidence of this interaction. In addition, although genome-wide association study analyses have implicated ADGRD1 SNPs in osteoporosis (*43*), the functional roles of these intronic SNPs remain to be clarified. It has been reported that macrophages and monocytes in the female reproductive system can regulate the functions of the ovary and other components of the oviductal system, which in turn play vital roles in bone mass regulation (*44*–*46*). Because the Lysm promoter in Lysm-Cre mice drives expression in monocytes and macrophages (*47*, *48*) and *Adgrd1* is also expressed in monocytes and macrophages (www.proteinatlas.org/search/adgrd1), it is reasonable to speculate that the female reproductive system with *Adgrd1* deficiency in monocytes and macrophages might regulate bone mass and osteoclast activity, which ultimately neutralizes the effect of *Adgrd1* in osteoclasts. Endogenous ligands of ADGRD1, such as PTK7 and PLXDC2, have been reported to be involved in diverse processes, including glioblastoma pathogenesis (*49*) and oviductal fluid flow during embryo transit (*50*). As an exogenous agonist, GL64 may influence the functions of these endogenous ligands in vivo. Single-cell sequencing data (from GSM3674242) revealed the high expression of *Ptk7* and *Plxdc2* in osteoclasts, osteoblasts, fibroblasts, and endothelial cells (fig. S10, A, C, and D). These findings suggest a potential role for ADGRD1 in mediating cell-cell communication within bone tissue, a function that GL64 may modulate.

MATERIALS AND METHODS

Mice

All experiments involving mice were approved by the East China Normal University (ECNU) Animal Care and Use Committee (ethical code: m20200407). The mice were housed under standard conditions, including a 12-hour dark-light cycle, constant temperature (20° to 26°C), and controlled humidity maintenance (40 to 60%), with ad libitum access to food and water. Both male and female mice were used in the experiments, except for the OVX model, in which only female mice were used.

Adgrd1 knockout mice (*Adgrd1*$^{-/-}$) were generated using the CRISPR-Cas9 system in the C57BL/6J mouse strain at the animal center of ECNU, which can be obtained from J.L. Briefly, exon 1 and exon 2 of the *Adgrd1* (ENSMUSG00000044017) transcript were recommended as the knockout region, guide RNAs (gRNAs) were designed in exon 1 and exon 2 (gRNA1, 5′-CGTTACCTGGACGCTGCAAA-3′; gRNA2, 5′-CCCAGAGCCCAGGAACATCC-3′), and then Cas9 mRNA and gRNA were microinjected into zygotes. Two weeks after birth, genomic DNA from the tail of the newborn F0 mice was extracted for sequencing. In detail, a 132–base pair (bp) segment, including an 82-bp intron sequence, was deleted between exon 1 and exon 2 of *Adgrd1*. Specifically, 18 bp of exon 1 were deleted, and 32 bp of exon 2 were deleted (fig. S4A). To confirm successful knockout, we performed genotyping of *Adgrd1* knockout mice using PCR (fig. S4C). There are three isoforms encoded by *Adgrd1* genes. Isoform 3 belongs to the "Retained intron" biotype and does not encode a functional protein, and isoform 2 lacks exon 4 (96 bp) compared with isoform1 (fig. S4B). We next evaluated the expression levels of *Adgrd1* isoforms 1 and 2 in knockout mice and did not detect the mRNA expression of *Adgrd1* isoforms 1 and 2 in *Adgrd1* knockout bone tissues (fig. S4D). Furthermore, immunofluorescence staining of bone sections confirmed that the Adgrd1 protein is deficient in *Adgrd1* knockout mice (fig. S4, E and F). These results demonstrated that the *Adgrd1* knockout mice were successfully constructed.

For conditional knockout mice, *Adgrd1*^{flox} mice were purchased from GemPharmatech (no. T009918). Briefly, two loxP sites were inserted upstream of exon 5 and downstream of exon 9 of *Adgrd1*, encompassing a 770-bp coding sequence. These mice were then crossed with Lysm-Cre mice (*7*, *29*–*32*) to generate *Adgrd1*$^{flox/flox}$, Lysm-Cre (*Adgrd1*^{Lysm}) mice (fig. S8A); Lysm-Cre mice (strain C57BL/6J) were donated by M.L. (*51*). Genotyping of *Adgrd1*^{Lysm} mice was performed using PCR (fig. S8B). In addition, we did not detect the mRNA expression of *Adgrd1* isoform 1 or 2 in osteoclasts isolated from male *Adgrd1*^{Lysm} mice (fig. S8C). Moreover, immunofluorescence staining of bone sections confirmed that the ADGRD1 protein was deficient in osteoclasts from *Adgrd1*^{Lysm} mice (fig. S8, D and E). These results demonstrated the successful generation of *Adgrd1* conditional knockout mice. The primer sequences for genotyping were as follows: for genotyping of *Adgrd1*$^{-/-}$ mice: 5′-TCTCCACCCAAAGCCAC G-3′ (forward) and 5′-TCTCAGCAGCAGCCCGAAG-3′ (reverse); for genotyping of *Adgrd1*^{Lysm} mice: 5′-AGCTGAG GTTG CA T A C A T G G AG-3′ (forward) and 5′-CCTTCT ATTAAT GTC AG G TC CAC G-3′ (reverse); for *Adgrd1*^{flox} mice: 5′-CCCAGAAATGCC A G AT TAC G-3′ (forward) and 5′-CTTGGGCTGCCAGAATTTCTC-3′ (reverse) for Lysm-Cre.

Ovariectomized mouse model

Twelve-week-old female C57BL/6J mice were purchased from the Experimental Animal Center of ECNU and randomly divided into three groups: sham, OVX, and OVX + GL64 ($n = 6$ per group). After anesthesia with tribromoethanol, the bilateral ovaries in the OVX groups were removed. Eight weeks postsurgery, the mice in the OVX + GL64 group were intraperitoneally injected with GL64 (30 mg/kg) daily, whereas those in the sham and OVX groups received daily intraperitoneal injections of DMSO (1% in normal saline). After a 4-week treatment period, all mice were euthanized.

Calvarial bones and femurs were collected for TRAP staining and microcomputed tomography (micro-CT) analysis.

Micro-CT

3D micro-CT analyses were performed as previously described (*30*). Sex- and age-matched femurs were analyzed using x-ray microtomography (Skyscan 1076, Bruker micro-CT) at a pixel size of 9 μm. After reconstruction, a region of interest of the distal femur was selected below the growth plate from 0.215 mm (1200 image slices) to 1.72 mm (1300 image slices), with the growth plate slice defined as 0 mm. 3D and BMD analyses were conducted using CTAn software (Bruker micro-CT), and 3D models were generated using CTVol software (Bruker micro-CT).

Virtual screening and molecule docking

Virtual screening was performed using the Schrödinger Suite (version 2020, Schrödinger, LLC, New York, NY). The cryo-EM structure of human ADGRD1 (*10*) was prepared using the Protein Preparation Wizard module in the Schrödinger Suite, which involved the removal of water molecules, the addition of missing hydrogen atoms, and the optimization of the protein geometry. Moreover, the internal agonist segment (*stachel* domain: TNFAILMQVV) was removed. A diverse set of commercial databases, including ChemDiv (containing 1,456,156 compounds) and Specs (containing 204,380 compounds) without pan-assay interference compounds (PAINS), was used for virtual screening. Ligands were prepared using the LigPrep module, which involved converting 2D structures to 3D structures, generating tautomers, and predicting the most likely ionization states at physiological pH (7.2). The receptor grid for docking was generated on the basis of the *stachel* domain binding pocket formed by the transmembrane domain. Glide, available in the Schrödinger Suite, was used for molecular docking. High-throughput virtual screening mode was initially used for the virtual screening of the entire compound database, after which the top-ranking ligands, based on their docking scores, were redocked in standard precision mode for enhanced accuracy. The compounds were ranked on the basis of their docking scores, and the top 1000 compounds were further analyzed for their interactions with the protein, predicted binding affinities, and drug-like properties. Subsequently, 79 hits were filtered on the basis of Lipinski's Rule of Five and other drug-like criteria to ensure optimal pharmacokinetic properties. The results of the virtual screening and the interactions between the selected hit compounds and ADGRD1 were visualized using PyMOL (The PyMOL Molecular Graphics System, version 2.0, Schrödinger, LLC).

MD simulations

To determine the MD simulations of the GL64-ADGRD1 system, the docked structure of the best scored binding pose was used as the initial structure. For the apo-ADGRD1 system, the cryo-EM structure of ADGRD1-CTF-Gs was used as the initial structure, with the CTF, Gs, and *stachel* sequences removed. Input files for both MD simulations were generated using the CHARMM-GUI server (*52*). The ADGRD1 structure was inserted into a POPC (palmitoyl-2-oleoyl-*sn*-glycero-3-phospho-choline) membrane, and TIP3P (transferable intermolecular potential with three points) water molecules were added to the top and bottom of the simulation systems. To neutralize the charge, 0.15 M NaCl was added using the Monte Carlo method. Neutral acetyl and methylamide groups were added to cap the N and C termini of ADGRD1, respectively. For both simulation systems, three independent 1-μs simulations were performed, with initial atom velocities assigned randomly and independently.

All MD simulations were performed using the GROMACS2020.2 package with the CHARMM36m force field (*53*). The parameters for the small molecule GL64 were generated using the CGenFF program (*54*). Before the final production run of the 1-μs MD simulations, each system underwent 50,000 steps of energy minimization followed by a 30-ns equilibration in the NPT ensembles. Positional restraints (1000 kJ mol^{-1} nm^{-2}) were applied to the heavy atoms of ADGRD1 and GL64 during equilibration. The system temperature was maintained at 310 K using the v-rescale method with a coupling time of 0.1 ps. The pressure was maintained at 1 bar using a Berendsen barostat, with a coupling time of 1.0 ps and a compressibility of 4.5×10^{-5} bar^{-1} with semi-isotropic coupling. A 2-fs time step and LINCS-constrained bond lengths were set during these simulations. Electrostatic interactions were computed using the particle mesh Ewald method, with nonbonded interactions cut at 1.2 nm. The results of the MD simulations were analyzed using GROMACS tools.

Reverse transcription and real-time PCR

Total RNA was extracted from primary murine osteoclasts or bone tissues using TRIzol reagent (Takara, 9109). The RNA was reverse transcribed into cDNA using HiScript II Q RT SuperMix (Vazyme R222-01). Real-time PCR analysis was performed on a real-time PCR system (QuantStudio Design & Analysis) using qPCR SYBR Green Master Mix (YEASEN, 11202ES03).

For the *Adgrd1* knockout mouse isoform 1 primer design, the forward primer was designed to pair with the excision site, and the reverse primer was designed to pair with the *Adgrd1* isoform 1–specific site (exon 4), which does not pair with *Adgrd1* isoform 2. For the *Adgrd1* knockout mouse isoform 2 primer design, the forward primer was designed to pair with the excision site, and the reverse primer was designed to pair with the *Adgrd1* isoform 2–specific site, which does not pair with *Adgrd1* isoform 1.

For the conditional knockout mouse isoform 1 primer design, the forward primer was designed to pair with the *Adgrd1* isoform 1–specific site (exon 4), which does not pair with *Adgrd1* isoform 2, whereas the reverse primer was designed to pair with the excision site. For the conditional knockout mouse *Adgrd1* isoform 2 primer design, the forward primer was designed to pair with the *Adgrd1* isoform 2–specific site, which does not pair with *Adgrd1* isoform 1, and the reverse primer was designed to pair with the excision site. The primers used for real-time PCR were as follows: *Nfatc1*: 5′-CCCGTCACATTCTGGTCCAT-3′ (forward) and 5′-CA A G T AACCGT GTAGCTGCACAA-3′ (reverse); *Dc-stamp*: 5′-TTTGCCGCTGTGGACTATCTGC-3′ (forward) and 5′-A G ACGTGG TTTAGGAATGCAGCTC-3′ (reverse); *Acp5*: 5′-CAGCTCCCTAGAAGATGGATTCAT-3′ (forward) and 5′-G TCA GG A G TGGGAGCCATATG-3′ (reverse); *Gapdh*: 5′-ACCCAGAAGACTGTGGATG-G-3′ (forward) and 5′-T TC A G C TCAGGGATGACCTT-3′ (reverse); *Adgrd1* isoform 1 (knockout mice): 5′-GTGTGTAGCA CTC AG CC CA GAG-3′ (forward) and 5′-AGAGGCACAGTGAGGTTGAGG-3′ (reverse); *Adgrd1* isoform 2 (knockout mice): 5′-GTGTGTAGCAC TCA GCCCA G AG-3′ (forward) and 5′-CCTTCCATGATATCTCCAGTTGTGT-3′ (reverse); *Adgrd1* isoform 1 (conditional knockout mice): 5′-CCTCAACCTCACT GTGCCTCT-3′ (forward) and 5′-TAGGAGGACCTCACCCACCG-3′ (reverse); *Adgrd1* isoform 2 (conditional knockout mice): 5′-ACACAA CTG GA GA T A T C A TGGAAGG-3′ (forward) and 5′-TAGGAGGACCTCA CCC AC CG-3′ (reverse).

Single-cell RNA sequencing

The single-cell RNA sequencing data were aligned and quantified using CellRanger software (version 7.1.0) with the GRCh38 human reference genome. The raw read count was subsequently processed using the Seurat package in R (version 4.0.5). Cells with <200 unique molecular identifiers or >15% mitochondrion-derived unique molecular identifiers were considered low quality and removed. The Seurat function ScaleData was used to correlate the effects of the cell cycle on the expression of cell cycle markers. Sctransform was subsequently performed to integrate five samples from different individuals into a shared space by removing batch effects while preserving biological variation. The main cell clusters were subsequently identified with the FindClusters function of Seurat, and the results were visualized using the uniform manifold approximation and projection method. Differentially expressed genes across cell clusters were identified with the FindAllMarkers function of Seurat.

Cell culture

To obtain BMMs, bone marrow cells were harvested from the tibiae and femurs of 6- to 8-week-old WT or *Adgrd1*$^{-/-}$ male mice. The cells were cultured for 1 day in α-minimum essential medium (α-MEM; Gibco, 12000022) supplemented with 10% fetal bovine serum (Gibco, 10099) and 1% penicillin/streptomycin. Nonadherent cells were transferred to a new plate, which was then treated with recombinant murine M-CSF (10 ng/ml; R&D, 416-mL-050) for 24 hours. To induce osteoclast differentiation, adherent BMMs were digested with Versene (Gibco, 15040066), seeded at a density of 1.5×10^4/cm^2, and cultured in α-MEM containing RANKL (100 ng/ml; R&D, 462-TEC) and M-CSF (10 ng/ml) for 6 days (*30*).

RAW264.7 cells were transfected with ADGRD1 plasmids using Fugene HD transfection reagent, as previously reported (*55*). The transfected cells were then treated with RANKL for 3 to 4 days. For the pit formation assay, mature osteoclasts were isolated as previously described (*55*) and stained with toluidine blue, and their pit perimeter, area, and depth were examined using laser-scanning confocal microscopy, as previously described (*56*).

TRAP staining

Mature osteoclasts cultured in 96-well plates were washed three times with phosphate-buffered saline (PBS), fixed with 4% paraformaldehyde (PFA) for 15 min, and permeabilized with 0.1% Triton X-100 for 10 min. The cells were then incubated for 30 min at 37°C with a TRAP staining kit (Sigma-Aldrich, 387A). For in vivo staining, paraffin sections were fixed in 4% PFA and then 0.1% Triton X-100 for 10 min, followed by incubation for 1 hour at 37°C with a TRAP staining kit. The osteoclast surface/bone surface (OC. S/BS), the number of osteoclasts/bone perimeter (N. OC/B. Pm), and the ES/BS 0.2 to 2 mm below the growth plate were analyzed using the OsteoMeasure Analysis System (Osteometrics, Decatur, GA) and ImageJ software (NIH) according to the manufacturers' protocols. For calvarial bone staining, TRAP staining was performed for 2 hours, and the osteoclast area was quantified using ImageJ software.

Scanning electron microscopy

WT and *Adgrd1* knockout BMM cells were treated with M-CSF (10 ng/ml) and RANKL (100 ng/ml) for 3 to 4 days on pits. The cells were fixed with glutaraldehyde and osmic acid, subjected to a dehydration gradient, and vacuum dried. The pits were sputter coated with gold for 30 s and visualized directly by scanning electron microscopy (SEM; JSM-5610).

Reporter gene assay

To identify the possible G proteins downstream of ADGRD1, a luciferase reporter gene system was used, as previously described (*57*). The cDNA sequence encoding human ADGRD1 (gene ID: 283383) isoform 1 was inserted into the pcDNA3.1(+) vector to generate an ADGRD1-overexpressed plasmid. For the luciferase assay, 5×10^4 HEK293T cells were seeded in 24-well plates, and the transfection was then performed when cells reach 70% confluency. A total of 1 μg of plasmids, including 200 ng of vector/ADGRD1, 780 ng of Cre-luciferase, and 20 ng of *Renilla* luciferase–expressing plasmids, was dissolved into 50 μl of serum-free Opti-MEM medium, mixed with a 50-μl mixture of Lipofectamine 2000 (Thermo Fisher Scientific, 11668019)/Opti-MEM medium (1:25) for 20 min, and then added into 24-well plates. After 24 hours of transfection, the cells were stimulated with GL64 or other agonists. The pharmacological compounds (table S1) were purchased from the Specs compound library (Zoetermeer, the Netherlands) and dissolved in DMSO to a concentration of 10 mM. Then, the agonists were serially diluted with 1× PBS and added to 24-well plates, followed by incubation for 24 hours before the luminescence recording was performed by using a Dual-Luciferase Reporter Assay System (Promega). Briefly, cells stimulated with GL64 or other agonists were lysed using passive lysis buffer (Promega, E1941) before receiving the Luciferase Assay Substrate (Promega, E151A) and Stop & Glo Substrate (Promega, E640A). The luminescence signal was then quantified using a Cytation 5 imaging reader (BioTek). The *stachel* peptide (TNFAILM QVV) targeting ADGRD1 was chemically synthesized by ChinaPeptides (Shanghai, China). *Stachel* peptides were suspended in DMSO at a concentration of 100 mM, and the cells were incubated with 1 mM peptide for 24 hours. For the CRE-luciferase assay in MEF cells, MEF cells were first isolated from WT and *Adgrd1*$^{-/-}$ embryonic mice. After one passage, 1×10^5 MEF cells were seeded into 24-well plates. Cre-luciferase plasmids and *Renilla* luciferase plasmids were cotransfected by using Lipofectamine 2000 when cells reach 70% confluency. Twenty-four hours posttransfection, MEF cells were stimulated with GL64 or the other agonists for 24 hours, with the luminescence signal quantified with a Cytation 5 imaging reader as described above.

cAMP concentration measured

cAMP enzyme-linked immunosorbent assay was measured following the manufacturer's protocol (CISBIO, 62AM4PEB). Briefly, MEF cells were isolated from WT and *Adgrd1*$^{-/-}$ embryonic mice and seeded into six-well plates at 5×10^5 cells per well. After 48-hour incubation, MEF cells were stimulated with GL64 for 1 hour, then harvested, and resuspended into a final cell density of 1×10^6 cells/ml in Hanks' balanced salt solution containing 500 μM IBMX. Ten microliters of cell suspension was transferred into standard 384-well plates at 1×10^4 cells per well, followed by the addition of lysis buffer containing 5 μl of cAMP-d2 and 5 μl of anti–cAMP-cryptate. After 1-hour incubation at room temperature in the dark, homogeneous time-resolved fluorescence signals were measured with a Cytation 5 Imagine Multi-Mode reader (BioTek, Winooski, VT).

Plasmid construction

The cDNA sequence encoding human ADGRD1 isoform 1 was synthesized by Youbao Company (Youbio, China). The cDNA sequence encoding human ADGRD1 (gene ID: 283383) isoform 1 was inserted into the pcDNA3.1(+) vector to generate the ADGRD1-overexpressed plasmid. Plasmids containing ADGRD1 mutations (S570A, Q616A, F623A, F643A, W705A, F716A, W773A, F791A, Q798A, H543A, F547A, I549A, L550A, M551A, and V553A) were generated by introducing these corresponding site-specific mutations into the human ADGRD1-encoding sequence within the pcDNA3.1(+) plasmid.

Immunofluorescence

After the paraffin was removed, the sections were permeabilized with 0.1% Triton X-100 and 0.1% PBS for 30 min, followed by antigen retrieval with proteinase K (20 μg/ml) for 20 min. The sections were then blocked with 2% bovine serum albumin for 1 hour and incubated overnight at 4°C with antibodies against TRAP (Rabbit, SAB, 32694, 1:200, US; Mouse, Novus, NB300-555, 1:200, US) and ADGRD1 (Abmart, PC16289, 1:100). The sections were subsequently washed and incubated with a fluorescent secondary antibody (Alexa Fluor 594, 1:200; Invitrogen, Carlsbad, CA) for 1 hour in the dark. Nuclei were counterstained with 4,6-diamino-2-phenyl indole (DAPI; 1 μg/ml; Sigma-Aldrich, D9542). 3D images were captured using an Olympus fluorescence microscope (Olympus Corporation, Tokyo, Japan) and quantified using ImageJ software.

For in vitro studies, BMM or RAW264.7 cells were induced with RANKL for 2 days on slides. After being removed from the medium and washed three times with PBS, the slides were fixed with 4% formaldehyde, permeabilized with 0.1% Triton X-100, blocked with 5% bovine serum albumin, and then incubated with a mouse anti-NFATC1 primary antibody (Santa Cruz, Sc-7294, 1:200, US) for 24 hours at 4°C. The slides were then incubated with a fluorescent secondary antibody for 1 hour in the dark and counterstained with DAPI (1 μg/ml). 3D images were taken using an Olympus fluorescence microscope (Olympus Corporation, Tokyo, Japan) and quantified using ImageJ software.

Histomorphometry

Calcein double labeling was performed by administering calcein (30 mg/kg) via intraperitoneal injection twice on postnatal day 30 (P30) and P40. The mice were euthanized on P47, and the vertebral bones were fixed in 4% PFA for 2 days and subsequently embedded in methylmethacrylate. Histomorphometry was conducted on plastic-embedded samples using standard protocols. Bone dynamic histomorphometric analyses were performed for BFR/BS (bone formation rate per bone surface) and mineral apposition rate. Static histomorphometric analyses were performed to quantify N. OB/B (the number of osteoclasts/bone), OS/BS (osteoid per bone surface), trabecular BV/TV, TB. N, TB.TH, and TB. SP using the Osteomeasure Histomorphometry System (OsteoMetrics, Decatur, GA).

Pharmacokinetics

Eight-week-old male mice were randomly divided into two groups (three mice per group). The mice were treated with GL64 (30 mg/kg) by intraperitoneal injection. At time points including 5 min, 30 min, 1 hour, 2 hours, 4 hours, and 8 hours, the first group of mice was anesthetized, followed by heart perfusion with saline, and then euthanized. Two hundred microliters of blood sample was collected from each mouse. The plasma was separated immediately by centrifugation at 5000 rpm for 5 min at room temperature and stored at −80°C until analysis. For the second group of mice, the bone marrow was homogenized and centrifuged at 10,000 rpm for 5 min, 1 hour, or 4 hours. The supernatant was collected and stored at −80°C until analysis. The concentrations of GL64 in the serum and bone marrow were evaluated by liquid chromatography–tandem mass spectrometry.

Statistics

Statistical analyses were performed using Prism 7.0 software (GraphPad Prism). The data are presented as the means ± SD. Statistical significance between two groups was determined using a two-tailed Student's *t* test, whereas a one-way or two-way analysis of variance (ANOVA) with Dunnett's test was used for multiple comparisons, as appropriate. A *P* value less than 0.05 was considered statistically significant.

Supplementary Materials

This PDF file includes:
Figs. S1 to S15
Tables S1 to S7

REFERENCES AND NOTES

1. M. Lu, B. Wu, Structural studies of G protein-coupled receptors. *IUBMB Life* **68**, 894–903 (2016).
2. A. S. Hauser, M. M. Attwood, M. Rask-Andersen, H. B. Schiöth, D. E. Gloriam, Trends in GPCR drug discovery: New agents, targets and indications. *Nat. Rev. Drug Discov.* **16**, 829–842 (2017).
3. NIH Consensus Development Panel on Osteoporosis Prevention, Diagnosis, and Therapy, Osteoporosis prevention, diagnosis, and therapy. *JAMA* **285**, 785–795 (2001).
4. N. J. Kapolka, G. J. Taghon, J. B. Rowe, W. M. Morgan, J. F. Enten, N. A. Lambert, D. G. Isom, DCyFIR: A high-throughput CRISPR platform for multiplexed G protein-coupled receptor profiling and ligand discovery. *Proc. Natl. Acad. Sci. U.S.A.* **117**, 13117–13126 (2020).
5. M. Hua, G. Peluffo, H. Chen, R. Gelman, S. Schnitt, K. Polyak, Role of COX-2 in epithelial-stromal cell interactions and progression of ductal carcinoma in situ of the breast. *Proc. Natl. Acad. Sci. U.S.A.* **106**, 3372–3377 (2009).
6. N. Tołoczko-Iwaniuk, D. Dziemiańczyk-Pakieła, B. K. Nowaszewska, K. Celińska-Janowicz, W. Miltyk, Celecoxib in cancer therapy and prevention - Review. *Curr. Drug Targets* **20**, 302–315 (2019).
7. P. Sun, L. He, K. Jia, Z. Yue, S. Li, Y. Jin, Z. Li, S. Siwko, F. Xue, J. Su, M. Liu, J. Luo, Regulation of body length and bone mass by Gpr126/Adgrg6. *Sci. Adv.* **6**, eaaz0368 (2020).
8. M. Wu, T.-H. Lo, L. Li, J. Sun, C. Deng, K.-Y. Chan, X. Li, S. T.-Y. Yeh, J. T. H. Lee, P. P. Y. Lui, A. Xu, C.-M. Wong, Amelioration of non-alcoholic fatty liver disease by targeting adhesion G protein-coupled receptor F1 (*Adgrf1*). *eLife* **12**, e85131 (2023).
9. W. An, H. Lin, L. Ma, C. Zhang, Y. Zheng, Q. Cheng, C. Ma, X. Wu, Z. Zhang, Y. Zhong, M. Wang, D. He, Z. Yang, L. Du, S. Feng, C. Wang, F. Yang, P. Xiao, P. Zhang, X. Yu, J.-P. Sun, Progesterone activates GPR126 to promote breast cancer development via the Gi pathway. *Proc. Natl. Acad. Sci. U.S.A.* **119**, e2117004119 (2022).
10. Y.-Q. Ping, P. Xiao, F. Yang, R.-J. Zhao, S.-C. Guo, X. Yan, X. Wu, C. Zhang, Y. Lu, F. Zhao, F. Zhou, Y.-T. Xi, W. Yin, F.-Z. Liu, D.-F. He, D.-L. Zhang, Z.-L. Zhu, Y. Jiang, L. Du, S.-Q. Feng, T. Schöneberg, I. Liebscher, H. E. Xu, J.-P. Sun, Structural basis for the tethered peptide activation of adhesion GPCRs. *Nature* **604**, 763–770 (2022).
11. A. L. Kierszenbaum, Epididymal G protein-coupled receptor (GPCR): Two hats and a two-piece suit tailored at the GPS motif. *Mol. Reprod. Dev.* **64**, 1–3 (2003).

12. A. Kishore, R. H. Purcell, Z. Nassiri-Toosi, R. A. Hall, Stalk-dependent and Stalk-independent signaling by the adhesion G protein-coupled receptors GPR56 (ADGRG1) and BAI1 (ADGRB1). *J. Biol. Chem.* **291**, 3385–3394 (2016).
13. L. M. Demberg, J. Winkler, C. Wilde, K.-U. Simon, J. Schön, S. Rothemund, T. Schöneberg, S. Prömel, I. Liebscher, Activation of adhesion G protein-coupled receptors. *J. Biol. Chem.* **292**, 4383–4394 (2017).
14. Y.-Q. Ping, C. Mao, P. Xiao, R.-J. Zhao, Y. Jiang, Z. Yang, W.-T. An, D.-D. Shen, F. Yang, H. Zhang, C. Qu, Q. Shen, C. Tian, Z.-J. Li, S. Li, G.-Y. Wang, X. Tao, X. Wen, Y.-N. Zhong, J. Yang, F. Yi, X. Yu, H. E. Xu, Y. Zhang, J.-P. Sun, Structures of the glucocorticoid-bound adhesion receptor GPR97-G complex. *Nature* **589**, 620–626 (2021).
15. N. S. Bayin, J. D. Frenster, J. R. Kane, J. Rubenstein, A. S. Modrek, R. Baitalmal, I. Dolgalev, K. Rudzenski, L. Scarabottolo, D. Crespi, L. Redaelli, M. Snuderl, J. G. Golfinos, W. Doyle, D. Pacione, E. C. Parker, A. S. Chi, A. Heguy, D. J. MacNeil, N. Shohdy, D. Zagzag, D. G. Placantonakis, GPR133 (ADGRD1), an adhesion G-protein-coupled receptor, is necessary for glioblastoma growth. *Oncogenesis* **5**, e263 (2016).
16. J. D. Frenster, J. F. Inocencio, Z. Xu, J. Dhaliwal, A. Alghamdi, D. Zagzag, N. S. Bayin, D. G. Placantonakis, GPR133 promotes glioblastoma growth in hypoxia. *Neurosurgery* **64**, 177–181 (2017).
17. G. Wu, D. Zhai, J. Xie, S. Zhu, Z. Liang, X. Liu, Z. Zhao, N^6-methyladenosine (m^{6}A) RNA modification of G protein-coupled receptor 133 increases proliferation of lung adenocarcinoma. *FEBS Open Bio* **12**, 571–581 (2022).
18. M. Lv, X. Li, W. Tian, H. Yang, B. Zhou, ADGRD1 as a potential prognostic and immunological biomarker in non-small-cell lung cancer. *Biomed. Res. Int.* **2022**, 5699892 (2022).
19. K. Zhu, A. Yan, F. Zhou, S. Zhao, J. Ning, L. Yao, D. Shang, L. Chen, A pyroptosis-related signature predicts overall survival and immunotherapy responses in lung adenocarcinoma. *Front. Genet.* **13**, 891301 (2022).
20. Y. F. Chan, F. C. Jones, E. McConnell, J. Bryk, L. Bünger, D. Tautz, Parallel selection mapping using artificially selected mice reveals body weight control loci. *Curr. Biol.* **22**, 794–800 (2012).
21. M. A. Jarboui, C. Bidoia, E. Woods, B. Roe, K. Wynne, G. Elia, W. W. Hall, V. W. Gautier, Nucleolar protein trafficking in response to HIV-1 Tat: Rewiring the nucleolus. *PLOS ONE* **7**, e48702 (2012).
22. A. Tönjes, M. Koriath, D. Schleinitz, K. Dietrich, Y. Böttcher, N. W. Rayner, P. Almgren, B. Enigk, O. Richter, S. Rohm, A. Fischer-Rosinsky, A. Pfeiffer, K. Hoffmann, K. Krohn, G. Aust, J. Spranger, L. Groop, M. Blüher, P. Kovacs, M. Stumvoll, Genetic variation in GPR133 is associated with height: Genome wide association study in the self-contained population of Sorbs. *Hum. Mol. Genet.* **18**, 4662–4668 (2009).
23. J.-J. Kim, Y.-M. Park, K.-H. Baik, H.-Y. Choi, G.-S. Yang, I. Koh, J.-A. Hwang, J. Lee, Y.-S. Lee, H. Rhee, T. S. Kwon, B.-G. Han, K. E. Heath, H. Inoue, H.-W. Yoo, K. Park, J.-K. Lee, Exome sequencing and subsequent association studies identify five amino acid-altering variants influencing human height. *Hum. Genet.* **131**, 471–478 (2012).
24. Y. K. Kim, S. Moon, M. Y. Hwang, D.-J. Kim, J. H. Oh, Y. J. Kim, B.-G. Han, J.-Y. Lee, B.-J. Kim, Gene-based copy number variation study reveals a microdeletion at 12q24 that influences height in the Korean population. *Genomics* **101**, 134–138 (2013).
25. L. He, Z. Xu, X. Niu, R. Li, F. Wang, Y. You, J. Gao, L. Zhao, K. M. Shah, J. Fan, M. Liu, J. Luo, GPRC5B protects osteoarthritis by regulation of autophagy signaling. *Acta Pharm. Sin. B* **13**, 2976–2989 (2023).
26. M. Z. Khan, L. He, Neuro-psychopharmacological perspective of Orphan receptors of Rhodopsin (class A) family of G protein-coupled receptors. *Psychopharmacology (Berl)* **234**, 1181–1207 (2017).
27. R. Ullah, Y. Shen, Y.-D. Zhou, K. Huang, J.-F. Fu, F. Wahab, M. Shahab, Expression and actions of GnIH and its orthologs in vertebrates: Current status and advanced knowledge. *Neuropeptides* **59**, 9–20 (2016).
28. C.-C. Hsiao, R. Sankowski, M. Prinz, J. Smolders, I. Huitinga, J. Hamann, GPCRomics of homeostatic and disease-associated human microglia. *Front. Immunol* **12**, –674189 (2021).
29. B. E. Clausen, C. Burkhardt, W. Reith, R. Renkawitz, I. Förster, Conditional gene targeting in macrophages and granulocytes using LysMcre mice. *Transgenic Res.* **8**, 265–277 (1999).
30. J. Luo, Z. Yang, Y. Ma, Z. Yue, H. Lin, G. Qu, J. Huang, W. Dai, C. Li, C. Zheng, L. Xu, H. Chen, J. Wang, D. Li, S. Siwko, J. M. Penninger, G. Ning, J. Xiao, M. Liu, LGR4 is a receptor for RANKL and negatively regulates osteoclast differentiation and bone resorption. *Nat. Med.* **22**, 539–546 (2016).
31. W. Zou, N. Rohatgi, T. H.-P. Chen, J. Schilling, Y. Abu-Amer, S. L. Teitelbaum, PPAR-γ regulates pharmacological but not physiological or pathological osteoclast formation. *Nat. Med.* **22**, 1203–1205 (2016).
32. M. Kittaka, T. Yoshimoto, C. Schlosser, R. Rottapel, M. Kajiya, H. Kurihara, E. J. Reichenberger, Y. Ueki, Alveolar bone protection by targeting the SH3BP2-SYK axis in osteoclasts. *J. Bone Miner. Res.* **35**, 382–395 (2020).
33. J.-W. Lee, B. X. Huang, H. Kwon, M. A. Rashid, G. Kharebava, A. Desai, S. Patnaik, J. Marugan, H.-Y. Kim, Orphan GPR110 (ADGRF1) targeted by N-docosahexaenoylethanolamine in development of neurons and cognitive function. *Nat. Commun.* **7**, 13123 (2016).
34. H. Y. Won, S. H. Mun, B. Shin, S.-K. Lee, Contradictory role of CD97 in basal and tumor necrosis factor-induced osteoclastogenesis in vivo. *Arthritis Rheumatol.* **68**, 1301–1313 (2016).
35. S. Hidaka, Y. Mouri, M. Akiyama, N. Miyasaka, K.-I. Nakahama, GPR110, a receptor for synaptamide, expressed in osteoclasts negatively regulates osteoclastogenesis. *Prostaglandins Leukot. Essent. Fatty Acids* **182**, 102457 (2022).
36. M. M. Weivoda, M. Ruan, C. M. Hachfeld, L. Pederson, A. Howe, R. A. Davey, J. D. Zajac, Y. Kobayashi, B. O. Williams, J. J. Westendorf, S. Khosla, M. J. Oursler, Wnt signaling inhibits osteoclast differentiation by activating canonical and noncanonical cAMP/PKA pathways. *J. Bone Miner. Res* **31**, 65–75 (2016).
37. G. Ramaswamy, H. Kim, D. Zhang, V. Lounev, J. Y. Wu, Y. Choi, F. S. Kaplan, R. J. Pignolo, E. M. Shore, Gsα controls cortical bone quality by regulating osteoclast differentiation via cAMP/PKA and β-catenin pathways. *Sci. Rep.* **7**, 45140 (2017).
38. M. M. Weivoda, M. Ruan, C. M. Hachfeld, L. Pederson, A. Howe, R. A. Davey, J. D. Zajac, Y. Kobayashi, B. O. Williams, J. J. Westendorf, S. Khosla, M. J. Oursler, Wnt signaling inhibits osteoclast differentiation by activating canonical and noncanonical cAMP/PKA pathways. *J. Bone Miner. Res* **34**, 1546–1548 (2019).
39. S.-H. Yoon, J. y. Ryu, Y. Lee, Z. H. Lee, H.-H. Kim, Adenylate cyclase and calmodulin-dependent kinase have opposite effects on osteoclastogenesis by regulating the PKA-NFATc1 pathway. *J. Bone Miner. Res.* **26**, 1217–1229 (2011).
40. S. R. Cummings, L. J. Melton, Epidemiology and outcomes of osteoporotic fractures. *Lancet* **359**, 1761–1767 (2002).
41. K. Andrade, J. Fornetti, L. Zhao, S. C. Miller, L. R. Randall, N. Anderson, S. E. Waltz, M. McHale, A. L. Welm, RON kinase: A target for treatment of cancer-induced bone destruction and osteoporosis. *Sci. Transl. Med.* **9**, eaai9338 (2017).
42. L. E. Surface, D. T. Burrow, J. Li, J. Park, S. Kumar, C. Lyu, N. Song, Z. Yu, A. Rajagopal, Y. Bae, B. H. Lee, S. Mumm, C. C. Gu, J. C. Baker, M. Mohseni, M. Sum, M. Huskey, S. Duan, V. N. Bijanki, R. Civitelli, M. J. Gardner, C. M. McAndrew, W. M. Ricci, C. A. Gurnett, K. Diemer, F. Wan, C. L. Costantino, K. M. Shannon, N. Raje, T. B. Dodson, D. A. Haber, J. E. Carette, M. Varadarajan, T. R. Brummelkamp, K. Birsoy, D. M. Sabatini, G. Haller, T. R. Peterson, *ATRAID* regulates the action of nitrogen-containing bisphosphonates on bone. *Sci. Transl. Med.* **12**, eaav9166 (2020).
43. J. A. Morris, J. P. Kemp, S. E. Youlten, L. Laurent, J. G. Logan, R. C. Chai, N. A. Vulpescu, V. Forgetta, A. Kleinman, S. T. Mohanty, C. M. Sergio, J. Quinn, L. Nguyen-Yamamoto, A.-L. Luco, J. Vijay, M.-M. Simon, A. Pramatarova, C. Medina-Gomez, K. Trajanoska, E. J. Ghirardello, N. C. Butterfield, K. F. Curry, V. D. Leitch, P. C. Sparkes, A. T. Adoum, N. S. Mannan, D. S. K. Komla-Ebri, A. S. Pollard, H. F. Dewhurst, T. A. D. Hassall, M.-J. G. Beltejar, 23andMe Research Team, D. J. Adams, S. M. Vaillancourt, S. Kaptoge, P. Baldock, C. Cooper, J. Reeve, E. E. Ntzani, E. Evangelou, C. Ohlsson, D. Karasik, F. Rivadeneira, D. P. Kiel, J. H. Tobias, C. L. Gregson, N. C. Harvey, E. Grundberg, D. Goltzman, D. J. Adams, C. J. Lelliott, D. A. Hinds, C. L. Ackert-Bicknell, Y.-H. Hsu, M. T. Maurano, P. I. Croucher, G. R. Williams, J. H. D. Bassett, D. M. Evans, J. B. Richards, An atlas of genetic influences on osteoporosis in humans and mice. *Nat. Genet.* **51**, 258–266 (2019).
44. Z. J. Zhang, L. Huang, L. Brayboy, Macrophages: An indispensable piece of ovarian health. *Biol. Reprod.* **104**, 527–538 (2021).
45. S. Younesi, S. J. Spencer, L. Sominsky, Monocyte perturbation modulates the ovarian response to an immune challenge. *Mol. Cell. Endocrinol.* **536**, 111418 (2021).
46. S. Khosla, D. G. Monroe, Regulation of bone metabolism by sex steroids. *Cold Spring Harbor Perspect. Med.* **8**, a031211 (2018).
47. X. Li, D. Liu, L. Zhao, L. Wang, Y. Li, K. Cho, C. Tao, B. Jiang, Targeted depletion of monocyte/macrophage suppresses aortic dissection with the spatial regulation of MMP-9 in the aorta. *Life Sci.* **254**, 116927 (2020).
48. D.-M. Yu, J. Zhao, E. E. Lee, D. Kim, R. Mahapatra, E. K. Rose, Z. Zhou, C. Hosler, A. El Kurdi, J.-Y. Choe, E. D. Abel, G. Hoxhaj, K. D. Westover, R. J. Cho, J. B. Cheng, R. C. Wang, GLUT3 promotes macrophage signaling and function via RAS-mediated endocytosis in atopic dermatitis and wound healing. *J. Clin. Invest.* **133**, e170706 (2023).
49. J. D. Frenster, H. Erdjument-Bromage, G. Stephan, N. Ravn-Boess, S. Wang, W. K. Liu, D. Bready, J. Wilcox, B. Kieslich, M. Jankovic, C. Wilde, S. Horn, N. Sträter, I. Liebscher, T. Schöneberg, D. Fenyo, T. A. Neubert, D. G. Placantonakis, PTK7 is a positive allosteric modulator of GPR133 signaling in glioblastoma. *Cell Rep.* **42**, 112679 (2023).
50. E. Bianchi, Y. Sun, A. Almansa-Ordonez, M. Woods, D. Goulding, N. Martinez-Martin, G. J. Wright, Control of oviductal fluid flow by the G-protein coupled receptor Adgrd1 is essential for murine embryo transit. *Nat. Commun.* **12**, 1251 (2021).
51. Z. Zhao, J. Qin, Y. Qian, C. Huang, X. Liu, N. Wang, L. Li, Y. Chao, B. Tan, N. Zhang, M. Qian, D. Li, M. Liu, B. Du, FFAR2 expressing myeloid-derived suppressor cells drive cancer immunoevasion. *J. Hematol. Oncol.* **17**, 9 (2024).
52. E. L. Wu, X. Cheng, S. Jo, H. Rui, K. C. Song, E. M. Dávila-Contreras, Y. Qi, J. Lee, V. Monje-Galvan, R. M. Venable, J. B. Klauda, W. Im, CHARMM-GUI toward realistic biological membrane simulations. *J. Comput. Chem.* **35**, 1997–2004 (2014).

53. J. Huang, S. Rauscher, G. Nawrocki, T. Ran, M. Feig, B. L. de Groot, H. Grubmüller, A. D. MacKerell Jr., CHARMM36m: An improved force field for folded and intrinsically disordered proteins. *Nat. Methods* **14**, 71–73 (2017).
54. K. Vanommeslaeghe, A. D. MacKerell Jr., Automation of the CHARMM General Force Field (CGenFF) I: Bond perception and atom typing. *J. Chem. Inf. Model.* **52**, 3144–3154 (2012).
55. C. Li, Z. Yang, Z. Li, Y. Ma, L. Zhang, C. Zheng, W. Qiu, X. Wu, X. Wang, H. Li, J. Tang, M. Qian, D. Li, P. Wang, J. Luo, M. Liu, Maslinic acid suppresses osteoclastogenesis and prevents ovariectomy-induced bone loss by regulating RANKL-mediated NF-κB and MAPK signaling pathways. *J. Bone Miner. Res.* **26**, 644–656 (2011).
56. B. K. McMichael, S. M. Meyer, B. S. Lee, c-Src-mediated phosphorylation of thyroid hormone receptor-interacting protein 6 (TRIP6) promotes osteoclast sealing zone formation. *J. Biol. Chem.* **285**, 26641–26651 (2010).
57. Z. Cheng, D. Garvin, A. Paguio, P. Stecha, K. Wood, F. Fan, Luciferase reporter assay system for deciphering GPCR pathways. *Curr. Chem. Genomics* **4**, 84–91 (2010).

Acknowledgments: We are grateful to all members of J.L.'s laboratory for technical help and discussion. **Funding:** This work is supported by grants from the National Key Research and Development Program of China (2023YFB3810200 to J.L., 2022YFC3400504 to J.S.), the National Natural Science Foundation of China (82225030, 92168204, and 9194910271 to J.L.; 82302778 to L.H.; and 32171130 to P.S.), the Fundamental Research Funds for the Central Universities (22120210586 to J.L. and 40500-20104-222592 to H.Y.), the Shanghai Municipal Health Commission Excellent Young Medical Talents Training Program (2022XD034 to J.L.), and the Innovative Research Team of High-level Local Universities in Shanghai (SHSMU-ZDCX20211201 to H.Y.). **Author contributions:** Conceptualization: J.L., H.Y., and M.L. Investigation: L.H., Y.L., Q.Z., Y.H., and Z.X. Writing—original draft: L.H., Q.Z., P.S., and N.W. Writing—review and editing: N.W., Q.Z., J.L., and H.Y. Project administration: J.L., H.Y., Y.S., and L.H. Funding acquisition: J.L., H.Y., L.H., and J.H. Supervision: H.Y., J.L., Y.S., and M.L. Methodology: J.S., Y.L., P.S., and S.Z. Resources: F.W., M.L., Y.Y., and Y.L. Validation: Y.Y., J.S., R.L., F.W., Z.X., and Y.H. Visualization: L.Z., Q.Z., and R.L. Formal analysis: Y.L., N.W., L.Z., J.-p.S., and S.Z. **Competing interests:** The authors declare that they have no competing interests. **Data and materials availability:** All data needed to evaluate the conclusions in the paper are present in the paper and/or the Supplementary Materials. Other key resources generated in-house, such as transgenic mouse lines, may be accessed by contacting J.L. (jluo@tongji.edu.cn).

Submitted 10 August 2024
Accepted 9 June 2025
Published 11 July 2025
10.1126/sciadv.ads3829